Journal of Quantitative Spectroscopy & Radiative Transfer 272 (2021) 107807

Contents lists available at ScienceDirect

Journal of Quantitative Spectroscopy & Radiative Transfer

journal homepage: www.elsevier.com/locate/jqsrt

CO-Ar collisions: *ab initio* model matches experimental spectra at a sub percent level over a wide pressure range

E.A. Serov[a,*], N. Stolarczyk[c], D.S. Makarov[a], I.N. Vilkov[a], G. Yu. Golubiatnikov[a], A.A. Balashov[a], M.A. Koshelev[a], P. Wcisło[c], F. Thibault[b], M. Yu. Tretyakov[a]

[a] *Institute of Applied Physics, Russian Academy of Sciences, 46 Ulyanov str., Nizhny Novgorod, 603950, Russia*
[b] *Univ Rennes, CNRS, Institut de Physique de Rennes, UMR 6251, Rennes F-35000, France*
[c] *Institute of Physics, Faculty of Physics, Astronomy and Informatics, Nicolaus Copernicus University in Torun, Grudziadzka 5, 87–100 Torun, Poland*

ARTICLE INFO

Article history:
Received 7 April 2021
Revised 4 June 2021
Accepted 14 June 2021
Available online 20 June 2021

Keywords:
Quantum scattering calculations
Line-shape parameters
Millimeter-wavelength range
BWO-based spectroscopy
Carbon monoxide
Wide pressure range

ABSTRACT

We use three independent spectroscopic techniques, operating in the millimeter-wavelength range, to study molecule-atom collisions, and validate our quantum-scattering calculations on two recent potential energy surfaces. We study the first pure rotational transition in a CO molecule perturbed by Ar. This molecular system is a good prototype of atmospherically relevant cases. It is, on the one hand, affordable for calculation of the line shape parameters by modern *ab initio* methods, and on the other hand, is very convenient for experimental studies because of its regular, well spaced rotational spectrum having a moderate intensity. We show that the simulated collision-perturbed spectra, which are based on our fully *ab initio* calculations, agree with the experimental line profiles at sub-percent level over a wide range (more than four orders of magnitude) of pressures. We demonstrate that the agreement between theory and experiment can be further improved if the model accounts for the collisional transfer of an optical coherence between different rotational transitions (the line-mixing effect). We show that the two surfaces tested in this work lead to a very similar agreement with the experiment. Capability of calculating line shape parameters in a broad range of temperatures is demonstrated.

1. Introduction

One of the major goals of molecular spectroscopy is the development of a model of radiation propagation, applicable to the widest possible range of spectral and thermodynamic conditions. Spectroscopic information accumulated and regularly updated in devoted databases and development of more and more sophisticated theoretical methods allow modeling of the observed spectra with a permanently increasing accuracy. In spectral intervals of single lines the experimental data can be reproduced with relative deviation down to 0.1 % or even better. However, such a good agreement is achieved, as a rule, by adjusting the number of line-shape parameters or, in other words, by fitting a theoretical model to experimental spectra. Moreover, the observed spectra can be distorted by various apparatus effects, which are modeled by introducing empirical functions having additional adjustable parameters. As a result, the parameters of the model retrieved from one experiment may not provide an agreement with another experimental data at the same level of accuracy. Such disagreements, however, are very small in comparison with cases where the line shape parameters are obtained by one or another interpolation and/or extrapolation method. Modern spectroscopic applications, such as, for example, remote sensing of planetary atmospheres, require parameters for billions of molecular lines at very different thermodynamic conditions, which is impossible to obtain from experiment. That is why simplified semi-empirical methods are widely used for calculating the line-shape parameters. Development of semi-empirical methods is complicated by difficulties in accurate representation of molecular collisions, which is known to be the crucial issue determining the shape of the observed molecular spectra [1,2]. Modeling of a collision requires knowledge of the full-dimensional intermolecular interaction potential. The *ab initio* methods of calculating the potential energy points for a multiplicity of mutual geometries of colliding molecules and further representation of the numerically obtained potential energy surface (PES) in functional form are known. A fairly good surface can now be produced in a reasonable time for relatively large molecular systems. However each particular case is still considered as a distinguished result. Moreover, even if the potential is known, accurate calculation of the molecular collision dynamics is a challenge for modern physics because any two colliding molecules are, in fact,

* Corresponding author.
E-mail address: serov@ipfran.ru (E.A. Serov).

https://doi.org/10.1016/j.jqsrt.2021.107807
0022-4073/

one multi-particle quantum system with many internal degrees of freedom.

We believe that one of the most promising approaches in resolving the problem of molecular collision characterization is the following. It is based on highly accurate interaction potential calculated *ab initio* by modern quantum chemical methods. The potential is used for determining the generalized spectroscopic cross sections on the basis of *ab initio* quantum scattering calculations [3–6]. At the next step, the numerical parameters quantifying various aspects of molecular collisions are derived from the cross sections. The retrieved parameters are verified by using them in the best available statistical model of the collision-perturbed shape of molecular lines [1,2,7–10], which is directly compared with high quality experimental data.

The success of this approach was recently demonstrated by the example of the simplest cases corresponding to collisions of H_2 with He [11–13], HD with He [14] and D_2 with D_2 [10]. To advance further in this direction, the approach was recently used for the study of collisions between the CO molecule and Ar based on the shapes of two and five rovibrational transitions in the P branch of the fundamental and second-overtone bands, respectively [15,16]. The unprecedented subpercent level of consistency between theory and experiment achieved in these studies evidences that *ab initio* calculations can provide reliable data for spectroscopic databases widely used by various applications. Note that CO lines are used in remote sensing as a fire smoke tracer and Ar is the third most abundant molecule in dry atmosphere.

In this work, we extend the previous studies on CO-Ar collisions [15,16] by exploring a different spectral regime in which other collisional effects can be observed. We study the collisional perturbation of the shape of the lowest rotational transition $j = 1 \leftarrow 0$ (R(0) line) in a CO molecule (colliding with Ar) in its ground vibrational state located in the 3-mm wavelength range. Such a choice allows us to exclude the influence of vibrational excitation and neglect centrifugal distortion thus focusing on the analysis of pure collisional effects including the line mixing, which did not manifest itself in the previous studies [15,16]. Another advantage of the selected spectral range is an easily achievable pressure range where the molecular dipole oscillation dephasing (relatively optical probe-radiation) due to the Doppler effect is negligible compared to the collisional dephasing (pure collisional regime). This allows one to disregard the Dicke narrowing and the correlations between velocity changing and dephasing collisions, which mask the manifestation of other collisional effects in the infrared range. We show that the simulated collision-perturbed spectra agree with the experimental line profiles at a sub-percent level over a wide range of pressures.

The regular well-spaced pure rotational spectrum of the CO molecule is very well studied both experimentally and theoretically. Line positions are known with sub-kHz accuracy from Lamb-dip measurements [17]. Pressure broadening, shifting and wind effect (speed dependence of collisional relaxation) of the spectrum were extensively studied [18–23]. The collisional coupling effect of CO lines perturbed by either Ar or He was explored only for the fundamental rovibrational band [24–27], the first [24,28] and the second [29] overtone band. To the best of our knowledge, the collisional effects manifesting themselves in the shape of pure rotational lines of the CO spectrum were never studied at elevated (near atmospheric) pressures.

For this study, we employ three different, by principle of operation, spectrometers with complementary abilities covering a pressure range from about 10 microbars up to 2 bars. This gives us a unique opportunity to release the quite common problem of systematic instrumental error if only one experimental setup is used. The broad pressure range allows continuous tracing of molecular line shape variation in the collisional regime under conditions changing from highly rarefied to dense gas.

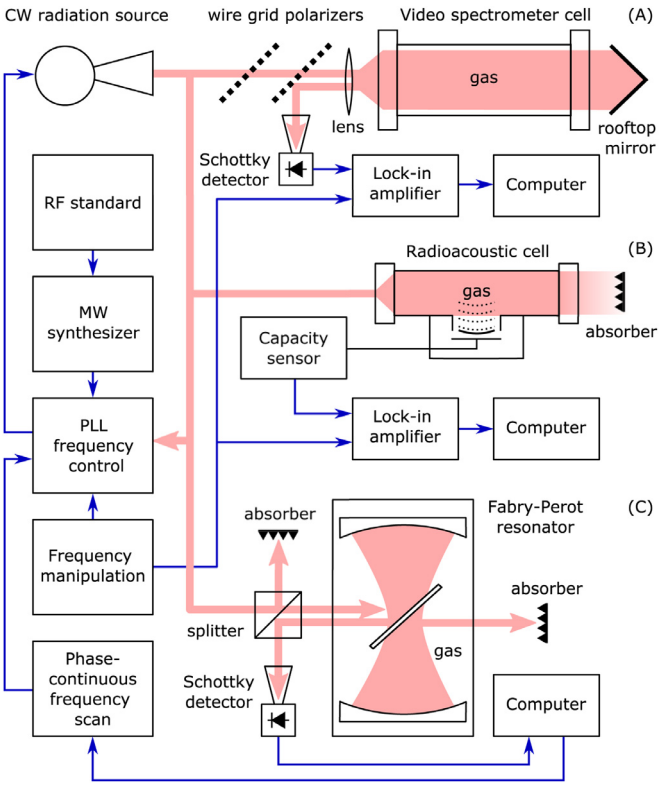

Fig. 1. Block diagram of the spectrometers used for measurements at various pressures. Section (A) shows the video spectrometer, section (B), the spectrometer with radioacoustic detection (RAD), and section (C), the resonator spectrometer.

The paper is organized as follows. Section 2 provides a brief description of the experimental setup and spectra acquisition. Section III presents details of the *ab initio* quantum-scattering calculations and line shape modeling. Comparison of theoretically calculated and experimental profiles is given and discussed in Section 4. The conclusions are summarized in Section 5. As a complementary work, Appendix A discusses the complex Dicke parameters and Appendix B provides the pressure broadening, pressure shift, complex Dicke parameters, and line mixing parameters for the R(0) line of CO in Ar over a wide range of temperatures.

2. Experiment

The unified diagram of our three spectrometers is presented in Fig. 1. All three setups utilize the continuous-wave, highly stable coherent radiation from a backward-wave oscillator (BWO) with the phase-locked loop (PLL) synchronization of the source frequency against the harmonic of the reference microwave synthesizer (HP8340B in the video spectrometer and Anritsu MG3692C in the radio-acoustic and the resonator spectrometers) synchronized with radio-frequency rubidium standard (GPS-12RG). The radiation power is about 10 mW. The radiation bandwidth is much less than 1 kHz, which allows neglecting the spectral resolution of the instrument in the absorption data analysis. More details on the radiation source and its precision digital frequency control can be found in [30] and references therein.

We used high-purity gases with natural isotopic composition from local suppliers. The declared gas purity was 99.995% for CO and 99.998% for Ar. Gas temperature in all experiments was maintained near room conditions and continuously monitored by several platinum sensors with 0.2 K uncertainty. Gas pressure

was measured by membrane sensors (MKS Baratron-626B, Inficon CDG0250 and Pfeiffer CCR-362) of the corresponding pressure range with declared accuracy of 0.2–0.25 % of reading.

Particular features of our spectrometers and experimental details are given in the next three subsections.

2.1. Video spectrometer

The direct absorption video spectrometer [31,32] was used for recording spectra at gas pressures of 10–500 mTorr (Fig. 1A). A beam of the linear-polarized millimeter-wave radiation formed by a horn antenna and a 20-cm focal length lens is directed to a stainless steel tube (2 m long and 11 cm in diameter) with high-density polyethylene windows serving as a gas cell. The radiation beam after the first pass of the cell is reflected back by the rooftop mirror (rotating radiation polarization by 90 degrees) and after the second pass is directed to the detector by a wire grid polarizer. A Schottky diode is used as a detector. The linear dependence of the detector output voltage *versus* radiation power was tested and calibrated. The radiation power was reduced to ~1 mW by the second wire grid polarizer in order to minimize the molecular transition saturation and the corresponding distortion of the absorption profile at low gas pressures. The gas absorption coefficient is determined using the well known equation derived from the Beer-Lambert-Bouguer law:

$$\alpha(\nu) = -\frac{1}{L_c} ln\left(\frac{P(\nu)}{P_0(\nu)}\right), \quad (1)$$

where P and P_0 denote the radiation power at frequency ν detected with and without absorbing gas, respectively ($P_0(\nu)$ is the baseline), and L_c is the absorption path length. The power recordings can be obtained by scanning the radiation source frequency through the desired range using radiation amplitude modulation (AM) and synchronous detection of the signal at the modulation frequency. The AM technique allows direct retrieval of the absorption profile by Eq. (1), but requires that the spectrometer baseline does not change during the measurement cycle. Providing the requested stability is not an easy task with the more than 4-m long radiation path. Even a small temperature-related variation of the radiation interference pattern or mean power may significantly distort the absorption profile. To reduce the baseline impact on the absorption shape, radiation frequency modulation (FM) is employed instead of AM. We use frequency manipulation or modulation by square wave form with preset deviation and synchronous detection at modulation frequency. This is achieved by using an arbitrary function generator (HMF2550) as the reference for the PLL system of the BWO. The recorded profile in this case is a difference of two true absorption profiles shifted up and down from the original one by the deviation frequency (finite difference derivative of the original profile). The smaller the frequency deviation, the less the baseline impact on the observed profile. The deviation values used in this study are less than 1 kHz. Even though for the final comparison with calculated absorption we selected the recordings for which the experimental perturbation of the baseline was the smallest.

2.2. Radioacoustic detection spectrometer

A spectrometer with radioacoustic detection of absorption (RAD) [33–36] was used for line profile studies in the pressure range 0.1–2 Torr (Fig. 1B). Radiation from the source is directed to the cell (copper tube with a diameter of 2 cm and a length of 10 cm) by a horn antenna. When molecules in the cell absorb radiation, their collisional relaxation leads to an increase in the temperature and pressure of the gas. If the amplitude of CW radiation is modulated by a periodic signal, the absorption causes respective pressure oscillations, *i.e.*, generates an acoustic wave, which is detected by a sensitive microphone and transformed into an electric signal by the resonance capacity sensor circuit. This signal is acquired using a lock-in amplifier referenced by the modulation frequency.

The acoustic signal S is directly proportional to the radiation power P_{abs} absorbed by the gas:

$$S \propto P_{abs} = P_0(\nu) - P(\nu) = P_0(\nu)(1 - e^{-\alpha(\nu)L_c}) \quad (2)$$

In this case, $P_0(\nu)$ and $P(\nu)$ denote the radiation power at the input and output of a gas cell, respectively. Under conditions of a low optical depth ($\alpha L_c \ll 1$, which is well satisfied for the CO line under study) and assuming that α does not depend on power, the output signal is directly proportional to the studied gas absorption coefficient and to the radiation power fed to the cell, $S \propto P_0\alpha(\nu)L_c$.

According to the principle of operation, the signal should appear only within the absorption lines and be absent outside the lines. However, a small baseline is present in this spectrometer due to the following technical reason: the absorption of radiation in the elements of the gas cell (mainly in the windows) leads to their heating and related secondary (nonradiative) heating of the gas, producing an additional acoustic signal.

Frequency manipulation with preset deviation (approximately equal to the half width at half maximum of the line under study) is employed, which leads to the reduction of the baseline effect and recording of absorption in the shape of a finite difference derivative of the original profile, as was described above in the video spectrometer subsection. Relatively small size of the cell and related radiation paths allow for good thermal and mechanical insulation, providing very stable experimental conditions. Experimental spectra are obtained by averaging of multiple recordings, which allows to reduce the instrumental noise. Back and forth frequency scanning around line center is used to minimize the effect of the instrumental time constant on the line center position.

2.3. Resonator spectrometer

The most wide-band recordings of the studied line in the CO–Ar mixture were obtained with a resonator spectrometer [37] (Fig. 1C). Two types of BWO were used as a sources, namely, OB-76 (frequency range 105–148 GHz) and OB-86 (frequency range 105–198 GHz). The absorption coefficient is retrieved from the change in the Fabry-Perot resonator Q-factor when it is filled with the studied gas. A high quality (Q-factor~ 10^6) resonator is placed inside the vacuum chamber equipped with the active temperature control system. The input and output windows of the chamber are produced from irradiated bulk polytetrafluoroethylene (PTFE) that has improved mechanical properties in comparison with the standard PTFE. The surfaces of the windows are corrugated using a special profile, which, in a manner similar to infrared and optical antireflective coatings, provides a low reflectivity of the windows in a wide frequency range [38].

The total pressure of the gas mixture ranged from 772 to 1525 Torr, while the relative fraction of CO varied from 3 to 14 %. The experimental conditions are listed in the Table 1. The CO and Ar densities were calculated from partial pressures using the virial equation of state and the data on the second virial coefficient [39,40]. The contribution of the third and subsequent terms of the virial equation expansion can be neglected under experimental conditions. Maximal relative difference between the calculated density and the corresponding ideal gas density was about 0.1%.

The baseline of the spectrometer, corresponding to the intrinsic resonator losses, was recorded when the chamber was filled with argon. The pressure of argon was chosen to provide the resonator optical length similar to that of the resonator filled with a mixture

Table 1
Resonator spectrometer experimental conditions.

#	T_{gas}, K	p_{CO}, Torr	p_{Ar}, Torr	n_{CO}, amg	n_{Ar}, amg	freq. range, GHz	exp. error, 10^{-8} cm^{-1}
1	297.4	24.91	747.4	0.03012	0.9038	105–148	0.5
2	296.6	49.82	747.9	0.06041	0.9069	105–148	0.7
3	296.8	74.74	747.5	0.09057	0.9058	105–148	1.6
4	296.4	124.6	747.9	0.1512	0.9075	105–198	1.6
5	297.5	124.6	995.2	0.1507	1.2034	105–198	2.5
6	296.9	125.3	1120	0.1518	1.3573	105–148	2.2
7	296.7	124.6	1245	0.1511	1.5107	105–148	2.3
8	297.7	124.6	1399	0.1506	1.6896	105–198	4.0

of CO and Ar with selected mixing ratio. The baseline was determined at the frequencies of sequential TEM_{00q} eigenmodes of the resonator by measuring their widths in the frequency domain. The interval between adjacent frequencies is 294 MHz. After the baseline recording, the chamber was evacuated and then filled with the desired amount of CO and then Ar. The gas mixing inside the chamber was accelerated by a fan. Reaching of equilibrium density was controlled by the time dependence of the width of the resonance mode located near the CO line center (∼115 GHz). As a rule, stable conditions were obtained in about one hour after the gas inlet when the resonance curve width reached a constant value within the statistical uncertainty.

The gas absorption coefficient was calculated from the formula

$$\alpha = \frac{4\pi}{c}(\Delta f_{gas} - \Delta f_{bln}), \tag{3}$$

where Δf_{gas} and Δf_{bln} are the resonance curve half widths at half maximum (HWHM), measured when the resonator is filled with studied mixture and non-absorbing gas, respectively.

The statistical uncertainty of the curve HWHM after averaging over 100 back and forth scans is about 8 Hz, which corresponds to the uncertainty of the absorption coefficient $5 \cdot 10^{-9}$ cm^{-1}. Additional uncertainty in the measured absorption is caused by parasitic reflections of radiation in the quasioptical-waveguide system, which is used for resonator excitation and registration of the resonance response. The reflection patterns are not exactly identical when the baseline and the studied gas spectrum are recorded. Hence, the obtained spectrum includes some systematic modulation of the resonance curve width, which depends on the distance between the quasioptical-waveguide system and the resonator. The effect is more pronounced the wider are the resonances. To reduce this effect, we averaged several spectra obtained for different positions of the quasioptical-waveguide system, as was described in detail in [37].

Thereby we obtain several individual spectra and the averaged spectrum for the desired conditions. An example of experimental spectrum (# 1, Table 1) obtained by averaging 4 individual recordings and 50×multiplied differences between the averaged spectrum and individual recordings are shown in Fig. 2. The scattering of individual spectra is somewhat larger than the aforementioned statistical uncertainty and amounts from $1.2{\cdot}10^{-8}$ cm^{-1} at line wings to $1.8{\cdot}10^{-8}$ cm^{-1} near the line centre. However, the real uncertainty of the averaged spectrum is sufficiently lower due to reducing the systematic effect of parasitic reflection of radiation by averaging of the recordings obtained at different phases of these reflections. The uncertainty can be estimated from the residual after fitting the proper model profile to the averaged spectrum. Before fitting the model to the R(0) line, the absorption of other CO lines contributing to the experimental spectrum was calculated and subtracted from experimental spectra (see Section 4 for details). If we take the van Vleck-Weisskopf model updated by inclusion of the line mixing and speed dependence of collisional relaxation (as is discussed in detail in Section 3) with the additional smooth pedestal corresponding to the CO-Ar continuum and fit it to the averaged experimental spectrum (Fig. 2), then the standard deviation of residual is $5 \cdot 10^{-9}$ cm^{-1}. Estimated uncertainties of all experimental recordings are given in Table 1.

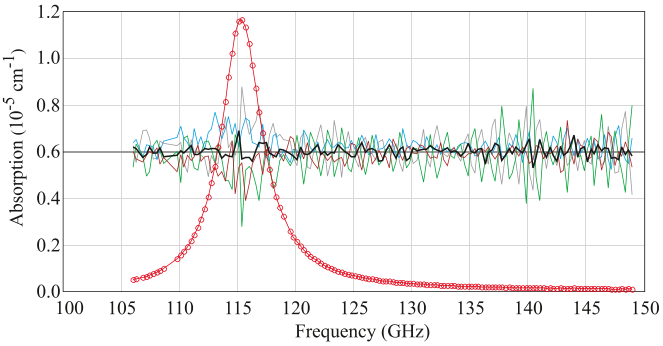

Fig. 2. Averaged experimental spectrum of a CO-Ar mixture at room temperature for p_{CO} = 24.91 Torr and p_{Ar} = 747.4 Torr (red line). Blue, green, brown and gray lines are the 50×multiplied differences between single records obtained at different distances between the quasioptical system and the resonator, and the averaged spectrum. Thick black line is the 50×(Exp− Fit.) residual for the model given by Eq. (26). All residuals are shifted up by $0.6 \cdot 10^{-5}$ cm^{-1} for clarity. (For interpretation of the references to colour in this figure legend, the reader is referred to the web version of this article.)

3. *Ab initio* quantum-scattering calculations and perturbation of the shape of molecular resonance

3.1. Quantum scattering calculation

Quantum dynamical calculations were performed on either the potential energy surface (PES) of Sumiyoshi and Endo [41] already used by some of us in [15,16,42] or a more recent one of Cybulski [16]. These two three-dimensional PESs, $V(r, R, \theta)$, where r is the CO intramolecular distance, R the distance between the CO centre of mass and the Ar atom, and θ the angle between $\vec{r}$ and $\vec{R}$, were first expanded in the basis of Legendre polynomials up to the 10th order:

$$V(r, R, \theta) = \sum_L V_L(r, R) P_L(\cos\theta). \tag{4}$$

Then the radial coupling terms, $V_L(r, R)$, were averaged over the CO rovibrational wave functions $\chi_{v,j}(r)$ in order to provide the rovibrational potential coefficients:

$$V_{L,vj,v'j'}(R) = \int_0^\infty \chi_{v'j'}(r) V_L(r, R) \chi_{vj}(r) dr, \tag{5}$$

where the subscripts v and j designate vibrational and rotational quantum numbers and vj, $v'j'$ are the states coupled by the PES. The $\chi_{vj}(r)$ functions were determined by using the DVR-FBR method (discrete variable representation — finite basis representation) on the CO potential of Murrell and Sorbie [43] updated by Huxley and Murrell [44]. We have checked that the centrifugal distortion has no effect, as well as vibrational coupling terms, thus we denote these terms $V_L(R)$ for $V_{L,00,00}(R)$. Scattering matrix elements relevant for the calculations of generalized spectroscopic collisional cross sections were obtained from close-coupling calculations using the non-reactive MOLSCAT code [45], or its parallelized version [46], for kinetic energies[1] between 0.1 to 2000 cm^{-1}. Other technical details regarding the use of MOLSCAT code for the system under study can be found in [15,16,42,47–52].

[1] All the energies are expressed in cm^{-1}, thus E stands for E/hc with h, the Planck constant, and c, the speed of light, in cm/s.

3.2. Generalized cross sections

Following the generalized Hess method (GHM) [53,54], the spectroscopic collisional cross sections are expressed as

$$\sigma_\lambda^q(j_i'j_f', j_ij_f; E_{kin}) = \frac{\pi}{k^2}(-1)^{(j_i+j_i')}\left(\frac{[j_i']}{[j_i]}\right)^{1/2} \times \sum_{J_iJ_f,\ell,\ell',\bar\ell,\bar\ell'} [J_i][J_f]\left([\ell][\ell'][\bar\ell][\bar\ell']\right)^{1/2}(i)^{-\ell+\ell'+\bar\ell-\bar\ell'} \times \begin{pmatrix}\ell & \bar\ell & \lambda\\ 0 & 0 & 0\end{pmatrix}\begin{pmatrix}\ell' & \bar\ell' & \lambda\\ 0 & 0 & 0\end{pmatrix}\begin{bmatrix} j_i & j_i' & \bar\ell & \bar\ell'\\ j_f & \ell & j_f' & \ell'\\ q & J_f & J_i & \lambda\end{bmatrix} \times [\delta_{j_ij_i'}\delta_{j_fj_f'}\delta_{\ell\ell'}\delta_{\bar\ell\bar\ell'} - \langle j_i\ell\left|S^{J_i}(E_{kin}+E_i)\right|j_i'\ell'\rangle\langle j_f\bar\ell\left|S^{J_f}(E_{kin}+E_f)\right|j_f'\bar\ell'\rangle^*]. \quad (6)$$

In Eq. (6), the vibrational quantum number have been omitted since we consider only the ground vibrational state. Primes indicate post-collisional values. In Liouville space such a cross section describes the coupling of a line $|if\rangle\rangle$ (for short) with a line $|i'f'\rangle\rangle$. The various ℓ and $\bar\ell$ relate to the end-over-end rotational energy of the interacting pair. The close coupling (CC) S-matrix elements are expressed in the total angular momentum representation, $\vec J$, which is conserved during a collision (*e.g.*, $\vec J_i = \vec j_i + \vec\ell$). They are evaluated for different total energies equal to the relative kinetic energy of the colliding pair plus the rotational energy. k is the modulus of the wave vector associated with that collisional energy, $E_{kin} = (\hbar k)^2/2\mu$, with μ being the reduced mass of the CO-Ar system. q stands for the tensor order of the radiation-matter interaction ($q = 0$, 1 and 2 correspond to isotropic Raman Q lines, electric dipole transitions, and anisotropic Raman or quadrupolar transitions, respectively). In addition, [X] stands for 2X+1, (: : :) refers to the 3-j symbol and $\begin{bmatrix}:::\\:::\end{bmatrix}$, to the 12-j symbol of the second kind [55]. Finally, λ is the rank of the velocity tensor.

It has been recognized [5,53,54,56,57] that for $\lambda = 0$, such a GHM cross section reduces to the standard spectroscopic cross section [58,59] as derived from the impact approximation and leading to the so-called relaxation matrix in the line space [60]. Therefore, the real and imaginary parts of these diagonal cross sections provide the collisional half-widths and shifts, while off-diagonal terms provide the usual line coupling terms.

Since the considered line lies in the millimeter-wave range we have to take into account both the couplings with the neighboring R lines and their "mirror" lines located at negative frequencies. The latter correspond to the "anti-resonant" contribution of the familiar VVW profile. A R(j) line involves a Δj=+1 optical transition while its mirror component involves a Δj = -1 transition [58], thus, we will denote it P(j+1). For later use we also remind the reader of the following relation :

$$\sigma_0^1(j_f'j_i', j_fj_i; E_{kin}) = \left(\frac{[j_i][j_f']}{[j_i'][j_f]}\right)^{1/2}\sigma_0^{1*}(j_i'j_f', j_ij_f; E_{kin}) \quad (7)$$

that can be derived from Eq. (6) and the unitarity of the S-matrix. This relation, valid for pure rotational lines, implies [58] in particular that the collisional width of a R(j) line equals the width of the P(j+1) line, and that the shifts of these lines are just the opposite.

The second kind of generalized Hess cross sections, tied to λ = 1, has recently been discussed in the literature [6,11,14,61]. Since the orientation and magnitude of the velocity may change in the course of a dephasing collision, this cross section is associated with the diffusion of the polarization of the spectral transition. Therefore, there is a first correlation between the velocity changing and dephasing collisions. This correlation appears naturally in Hess [3] theory.

3.3. Off-diagonal relaxation matrix elements

The standard off-diagonal cross sections merit to be separately discussed, since we used different methods in order to determine them. Since we are only interested in the R(0) line at low or moderate pressures, it is fortunately not useful to calculate a full relaxation matrix [60]. Due to their high computational cost, we have only calculated the CC σ_0^1(R($j = 0-5$);R(0);E_{kin}) and σ_0^1(P($j = 1-4$);R(0);E_{kin}) cross sections for kinetic energies between 0.1 and 2000 cm^{-1}. To complete (for $j \geq 5$) these sets of non-diagonal cross sections we made use of the energy corrected sudden approximation (ECSA) (for a review see Ref. [62]).

The ECSA exploits an inelastic cross section out of $j = 0$ (or of cross sections from $j' \neq 0$ to $j = 0$ using the micro-reversibility). This allows one to express all non-diagonal generalized cross sections in terms of such standard state-to-state cross sections, $\sigma(L \equiv j \to 0)$, where it is customary [62] to replace j by L, via

$$\sigma_0^q(j_i'j_f', j_ij_f; E_{kin}) = -\left(\frac{[j_i']}{[j_i]}\right)^{1/2} \sum_L [L]F^q(j_i'j_f', j_ij_f; L)\frac{\sqrt{\Omega_{j_i}\Omega_{j_f}}}{\Omega_L}\sigma(L\to 0; E_{kin}) \quad (8)$$

Here, the Percival-Seaton spectroscopic coefficients are given by

$$F^q(j_i'j_f', j_ij_f; L) = (-1)^q\left([j_i][j_i'][j_f][j_f']\right)^{1/2} \times \begin{pmatrix} j_i & L & j_i'\\ 0 & 0 & 0\end{pmatrix}\begin{pmatrix} j_f & L & j_f'\\ 0 & 0 & 0\end{pmatrix} \times \begin{Bmatrix} j_i & j_f & q\\ j_f' & j_i' & L\end{Bmatrix}, \quad (9)$$

where {:::} denotes a 6j symbol. In fact, since $j_i = 0$ by virtue of the triangular rule, implied by the first 3-j symbol, there is only one L value for the R(0) line, with $L = j_i'$ that contributes to the summation.

The Ω's adiabaticity factors, figuring in Eq. (8), were first introduced by DePristo et al. [63] to correct for the sudden approximation. Based on our previous studies on CO_2 – Ar [64] and CO – Ar [26], we have preferred to use the form of these factors proposed by Bonamy et al. [65]:

$$\Omega_j = \left[1 + \frac{1}{12}\left(\omega_{j,j-1}\tau_c\right)^2\right]^{-1}, \quad (10)$$

where τ_c is the effective duration of a collision and $\omega_{j,j-1}$ is the angular frequency spacing between adjacent levels. The relaxation matrix elements (in cm^{-1}) are deduced from a Maxwell-Boltzmann thermal average of these cross sections,

$$\langle\langle l'|W|l\rangle\rangle = \frac{n_{Ar}\bar v_r}{2\pi c}\langle\sigma_0^1(l', l; E_{kin})\rangle \quad (11)$$

where $|l\rangle\rangle$ and $|l'\rangle\rangle$ stand for the $|if\rangle\rangle$ and $\left|i'f'\right\rangle\rangle$ lines, respectively, $\bar v_r$ is the mean relative speed at a given temperature T, n_{Ar} is the number density of the bath composed of argon, and

$$\left\langle\sigma_0^1(l', l; E_{kin})\right\rangle = \frac{1}{(k_BT)^2}\int_0^\infty E_{kin}e^{-E_{kin}/k_BT}\ \sigma_0^1(l', l; E_{kin})\ dE_{kin}. \quad (12)$$

Finally, the relaxation matrix elements that obey the detailed balance principle, $W_{l'l}\cdot\rho_l = W_{ll'}\cdot\rho_{l'}$, where the ρ's are the thermal equilibrium populations of the initial level of the optical transition, are given by

$$W_{l'l} = -\frac{n_{Ar}}{2\pi c}\frac{\rho_{i_>}}{\rho_{j_i}}[i_<]\left([j_i]\left[j_i'\right]\right)^{-1/2}\left(\Omega_{i_>}\Omega_{f_>}\right)^{1/2} \times \sum_{L\neq 0}[L]F^1(j_i'j_f', j_ij_f; L)\frac{1}{\Omega_L}\mathcal{R}(L\to 0;T) \quad (13)$$

with $\mathcal{R}(L\to 0;T)$, the rate constant associated with the downward cross sections $\sigma(L\to 0)$. In the line shape literature, this rate is often expressed in terms of the so-called "basic rates" : $\mathcal{R}(L\to 0;T)\equiv \bar{\nu}_r Q_L'(T)$, where $Q_L'(T)$ is actually the thermally averaged cross section:

$$Q_L'(T) = \frac{1}{(k_BT)^2}\int_0^\infty E_{kin}\ e^{-E_{kin}/k_BT}\ \sigma(L\to 0;E_{kin})\ dE_{kin}. \quad (14)$$

In Eq. (13), $i_>$ ($i_<$) and $f_>$ stand for the maximum (resp. minimum) value of (j_i, j_i') and (j_f, j_f'). Thus, to generate the necessary off-diagonal relaxation matrix elements we only need to have at our disposal the downward rates to $j = 0$ or equivalently the basic rates $Q_L'(T)$. Thanks to our scattering calculations over a large grid of kinetic energies, we have in fact $\sigma(L\to 0;E_{kin})$, and thus the rate constants $\mathcal{R}(L\to 0;T)$ up to $L = 20$.

In addition, in Ref. [26], the basic rates were modeled using a hybrid exponential-power (EP) law [66]:

$$Q_L'(T) = \frac{A(T)}{[L(L+1)]^\alpha}\ e^{-\beta\frac{E_L}{k_BT}}. \quad (15)$$

The adjustable parameters, A, α, and β, are given in Table V of Ref. [26]. From this table the effective duration τ_c, at room temperature T, of a collision can also be easily deduced.

To conclude this section, we have therefore three sets of relaxation matrix elements: a limited set obtained from our *ab initio* CC calculations and including the couplings of the R(0) line with its 5 neighbouring R lines and the couplings with the P(1) to P(4) lines located at negative frequencies, a second set coming from our mixed CC/ECSA calculations, and a third one derived from the fitted basic rates of Ref. [26].

3.4. Line-shape parameters

It is well known [62] that the real and (minus) imaginary parts of the diagonal relaxation matrix elements are the standard collisional Lorentzian halfwidth and shift parameters of a line:

$$\Gamma_{0,l} = Re(W_{ll}), \quad (16)$$

$$\Delta_{0,l} = -Im(W_{ll}). \quad (17)$$

In the first order with respect to pressure, to the Lorentzian line profile a dispersive contribution that comes from the line mixing must be added. This dispersive component is characterized by the Rosenkranz [67,68] line mixing parameter

$$Y_l = 2\sum_{l'\neq l}\frac{d_{l'}}{d_l}\frac{W_{l'l}}{\nu_l-\nu_{l'}}, \quad (18)$$

where d_l is the reduced dipole matrix element for the line $|l\rangle$,

$$d_l = (-1)^{j_f}\left[j_f\right]^{1/2}\begin{pmatrix} j_f & j_i & 1\\ 0 & 0 & 0\end{pmatrix}, \quad (19)$$

and ν_l denotes its position in the spectrum in cm^{-1}. As for rovibrational spectra having regular R and P branches we can split Eq. (18) into two contributions:

$$Y_l = 2\sum_{l'_+\neq l}\frac{d_{l'_+}}{d_l}\frac{W_{l'_+l}}{\nu_l-\nu_{l'_+}} + 2\sum_{l'_-}\frac{d_{l'_-}}{d_l}\frac{W_{l'_-l}}{\nu_l-\nu_{l'_-}}, \quad (20)$$

the first contribution being associated with the intra-branch couplings, *i.e.*, R lines located at positive frequencies, and the second one with the inter-branch couplings, *i.e.*, P lines at negative frequencies.

Since $\Gamma_{0,l}$, $\Delta_{0,l}$, and Y_l are proportional to the number density of the bath gas, these parameters, normalized by the bath gas pressure, are widely used as spectroscopic coefficients:

$$\Gamma_{0,l} = p\gamma_{0,l} \quad (21)$$

$$\Delta_{0,l} = p\delta_{0,l} \quad (22)$$

$$Y_l = py_l. \quad (23)$$

Note that $Y_l = \left(Y_l^r + iY_l^i\right)$ is a complex line-mixing parameter. In the following discussion we limit our focus to the parameters concerning the R(0) line; therefore, we omit the line-count subscript l for simplicity.

The speed dependence of the line-shape [1,2] parameters also affects the line profile. Due to our quantum dynamical calculations for various energies we are in a position to provide the absolute active molecule speed dependence of the above parameters,

$$\Gamma(\nu) + i\Delta(\nu) = \frac{n}{2\pi c}\frac{2}{\sqrt{\pi}\bar{\nu}_p}\int_0^\infty d\nu_r\nu_r^2 e^{-\frac{\nu^2+\nu_r^2}{\bar{\nu}_p^2}}\sinh\left(\frac{2\nu\nu_r}{\bar{\nu}_p^2}\right)\sigma_0^q(\nu_r), \quad (24)$$

where n is the number density of the bath molecules, ν, ν_r and $\bar{\nu}_p$ are the speed of the active molecule, relative absorber-to-perturber speed and most probable perturber speed. Note that Eq. (24) deals with the diagonal cross section of the line under consideration. The same equation can be utilized to determine the speed dependence of the off-diagonal relaxation matrix elements and, thus, to derive the speed dependence of the line mixing parameter. The latter was evaluated and found to be negligible under our experimental conditions in accordance with conclusions of work Ref. [69]. The use of the speed dependent parameter $Y(\nu)$ instead of the speed averaged value Y in calculations of the line shape (Eq. (26)) leads to variations at the level of about 2×10^{-11} cm^{-1}, which is 160 times lower than the resonator spectrometer sensitivity. So in what follows we report only the speed averaged value of the line mixing.

3.5. The results of the quantum scattering calculations

Fig. 3 presents kinetic energy dependent pressure broadening and shift cross sections (top panels), as well as the off-diagonal cross sections (middle panels) for $\sigma_0^1(R(j=1-5);R(0);E_{kin})$ cross sections. Similar calculations (not shown) were performed for $\sigma_0^1(P(j=1-4);R(0);E_{kin})$ cross sections (as well as for the diagonal elements of the P(1) line located at negative frequency). The pressure-normalized, speed-dependent collisional half-width and shift of the R(0) line at 297.5 K are plotted in the bottom panels of Fig. 3. The thermally averaged relaxation matrix elements at 297.5 K related to the R(0)-R($j'\neq 0$) off diagonal cross sections are shown in Fig. 4 where they are compared with our mixed CC/ECSA values and the fitted ECS values [26].

Having at our disposal various sets of relaxation matrix elements we are in position to determine the line mixing parameter of the R(0) line at 297.5 K. In the following, for short, we call Y_{++} and Y_{+-} the contributions of the intra- and inter-branch couplings (Eq. (20)). Using the CC relaxation matrix elements between the R(0)-R(j=1-5) lines, we found the value Y_{++}= 6.87 × 10^{-3} atm^{-1} while the R(0)-P(j=1-4) relaxation matrix elements lead to Y_{+-}= -1.83 × 10^{-3} atm^{-1}. Thus, our CC initial value for the line mixing parameter is $y = 5.04\times 10^{-3}$ atm^{-1}. In the second step, in order to include more terms in the summation (Eq. (20)) leading to this parameter, we have included higher off-diagonal ECSA relaxation matrix elements derived from our present set of CC rate constant $\mathcal{R}(L\to 0;T)$ up to $L = 20$, thus including line mixing terms up to

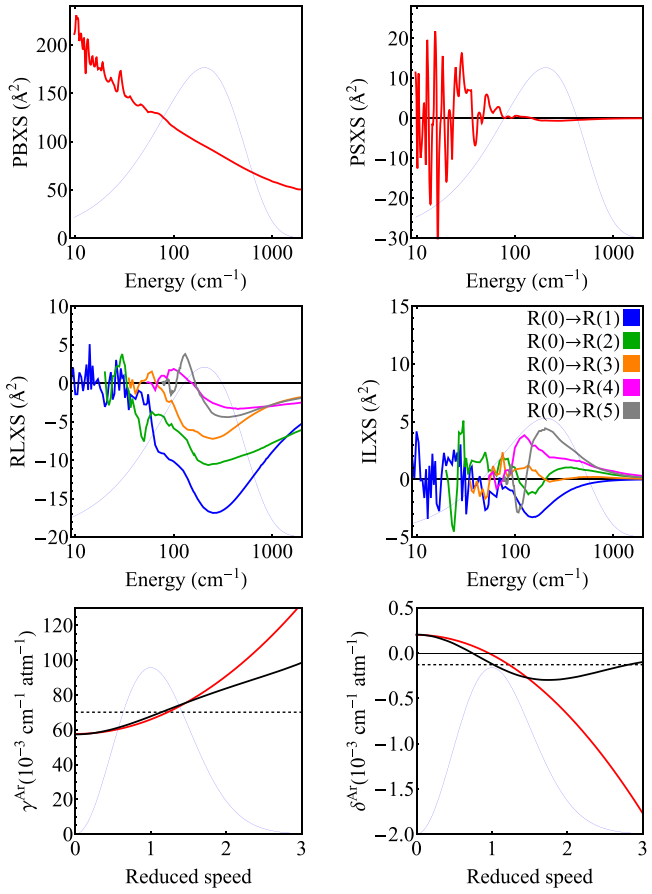

Fig. 3. *Ab initio* calculation results for the CO-Ar collisional system: top and middle panels: Pressure broadening and pressure shift cross sections (PBXS and PSXS), real and imaginary parts of the line mixing cross sections (RLXS and ILXS). Thin blue lines mark the Maxwell-Boltzmann distribution of the kinetic energy of perturber (Ar) molecules. Bottom panels: reduced speed (v/v_m) dependence of pressure broadening ($\gamma^{Ar} = \Gamma^{Ar}/p^{Ar}$) and shifting ($\delta^{Ar} = \Delta^{Ar}/p^{Ar}$) coefficients. Black curves are the *ab initio* data and red curves stand for the quadratic approximation. Dashed horizontal lines mark the speed-averaged values with respect to the Maxwell-Boltzmann speed distribution (thin blue lines). The results presented in this figure were calculated with Cybulski's PES [16]. (For interpretation of the references to colour in this figure legend, the reader is referred to the web version of this article.)

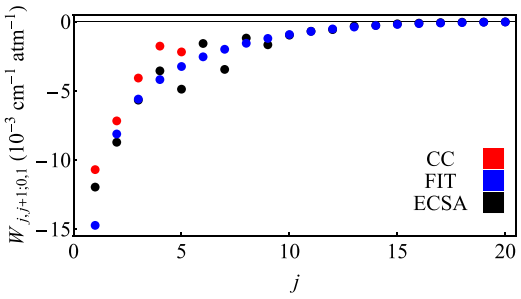

Fig. 4. Real part of relaxation matrix elements normalized by bath gas pressure coupling the line R(0) to the R(1) to R(20) lines calculated at 297.5 K. Full CC: red symbols; ECSA from our CC downward rates $\mathcal{R}(j \to 0; T)$: black symbols; fitted values [26]: blue symbols. Note that the blue and black dots overlay for $j \geq 10$. (For interpretation of the references to colour in this figure legend, the reader is referred to the web version of this article.)

Table 2
Ab initio spectral line-shape parameters for the CO-Ar collisional system calculated with the PES of Cybulski [16] and Sumiyoshi [41]. The calculations were performed for T = 297.5 K and the broadening and shifting coefficients are expressed in units of 10^{-3}cm^{-1}atm^{-1}, while the units of the line mixing are 10^{-3}atm^{-1}. The last column presents relative differences between the coefficients originating from the different PESs.

coefficients	Cybulski PES	Sumiyoshi PES	difference (%)
γ_0^{Ar}	69.7	70.9	1.7
δ_0^{Ar}	-0.13	-0.15	13
γ_2^{Ar}	8.2	8.7	5.7
δ_2^{Ar}	-0.22	-0.19	16
y^r	5.04	-	-
y^i	0.01	-	-

the R(20) and P(20) lines. This leads to a final value of 4.71× 10^{-3} atm^{-1}. Note that using the fitted rates [26] instead of the present rates leads to a close value of 4.82 × 10^{-3} atm^{-1}. This is not surprising because, at room temperature, taking into account the line mixing with the nine neighbouring lines (P(4) to R(5)) provides the main contribution to this parameter and the above values converge to better than 2 %, retaining the intra- and inter-branch coupling terms up to $j = 10$. In addition, one can see in Fig. 4 that the present ECSA set and the previous fitted one are indeed very close for L greater than about 8. Anyway, it is difficult to claim that our final value of the line mixing parameter is accurate to better than 7%. Indeed, the use of our present CC rates in conjunction with the ECSA, leads to the value of 4.7 × 10^{-3} atm^{-1}. This remarkable agreement with our final value is accidental because the separate contributions from the intra- and inter "branch are in fact quite different (Y_{++}=8.81 and $Y_{+-} = -4.11$, in 10^{-3} atm^{-1}). Nevertheless, our prediction of the line mixing parameter is also comparable to experimental or more or less accurately calculated values for the R(0) line of CO in various baths [24,27,28,70].

Finally, the relaxation matrix has complex-valued elements. Thus, we should be theoretically able to provide the imaginary part of the line mixing coefficient of the R(0) line. Indeed, our *ab initio* CC W(R(j=1-5;R(0)) have an imaginary part (right middle panel of Fig. 3) as well as the W(P(j=1-4;R(0)) leading to the total value 0.01 × 10^{-3} atm^{-1} for the imaginary part of this coefficient. Due to the largely predominance of the couplings with the first 9 neighbouring lines this certainly gives a correct order of magnitude of this part. Of course, since $Q_L'(T)$ are real, it is not possible to extrapolate using the ECSA. The absolute value of this imaginary part is much lower than the real part and has thus been neglected in the line shape analysis.

As a last remark, we point out that the present calculation of the line mixing parameter was done with Cybulski's PES [16]. Comparing the state-to-state cross sections out of $j = 0$ ($\sigma(j = 0 \to j'; E_{kin})$), the spectroscopic cross sections and the thermally averaged values obtained with the two used PESs [16,41], we have no doubt that Sumiyoshi *et al.* PES will lead to a very similar value of the line mixing parameter.

The thermally averaged, at 297.5 K and pressure-normalized line-shape parameters derived from the present *ab initio* calculations are gathered in Table 2. Appendix B provides their temperature dependence.

3.6. The model of a collision-perturbed shape of molecular resonance

The center frequency, ν_0, of the R(0) line of CO in the ground vibrational state equals 3.845033413(16) cm^{-1} [17]. The contribution of the Doppler broadening effect is quantified by its HWHM [71],

$$\Gamma_D = \nu_D\sqrt{\ln(2)} = \frac{\nu_0}{c}\sqrt{\frac{2k_BT}{m}\ln(2)}, \tag{25}$$

where $\nu_D = \nu_0\frac{v_m}{c}$ is the most probable Doppler shift, k_B, T and m are Boltzmann constant, temperature, and mass of the active molecule, respectively. In the case of the R(0) 0-0 line studied in

Table 3
Comparison of the speed-averaged CO-Ar collisional pressure broadening parameter values in different pressure ranges. The Doppler HWHM Γ_D value is 4.49 × 10^{-6}cm^{-1} at 296 K.

device	pressure range	Γ_0^{Ar} range [cm^{-1}]
resonator	772–1525 Torr	(7.08- 14.0)×10^{-2}
RAD	634–2049 mTorr	(5.79 - 18.7)×10^{-5}
VID	93.4–221.8 mTorr	(8.55 - 20.3)×10^{-6}

this paper, $\Gamma_D = 4.49 \times 10^{-6}$ cm^{-1} at 296 K. On the other hand, the collisional broadening parameter, Γ_0 scales linearly with pressure p.

Within this study we performed measurements in a wide pressure range, which affected the ratio between Γ_D and Γ_0. Table 3 presents the values of Γ_0 parameters in each of our three pressure ranges. While in the high-pressure regime Γ_0 dominates over Γ_D by at least two orders of magnitude, the parameters become commensurable in the intermediate- and low-pressure regimes. The Γ_0/Γ_D ratio determines the choice of a proper spectral line shape profile that we use to compare theoretical calculations with experimental data from each of the three spectrometers.

3.6.1. High-pressure collisional regime

This section describes the line-shape model used to simulate the theoretical spectra that we compare with the resonator spectrometer data. The contribution of the Doppler broadening effect is negligible compared to the collisional broadening, see Table 3. We can also disregard the influence of the velocity-changing collisions. To justify this we compared the speed-dependent Hard Collision profile [1] and the speed-dependent Lorentz profile. In our high pressure range, the two models differ on the level of 0.06%, which is much smaller than the other systematic uncertainties, in particular the one related to the choice of PES. Since we analyze the line in the microwave spectral range at high pressure, we have to take into account the influence of the radiation-term-related scaling factor proportional to ν^2/ν_0^2, as well as the slope coming from the negative-frequency peak (ignoring these two effects would make the residuals four times higher). A line-shape model which includes these two effects is called the van Vleck-Weisskopf (VVW) profile [72]. A modified version of the original VVW profile, including the line mixing and speed dependence of collisional broadening and shift can be expressed as [67,73]

$$I(\nu) = 4\pi^{-\frac{3}{2}} Re\left(\left(\frac{\nu}{\nu_0}\right)^2 \int_0^\infty e^{-x^2} x^2 \left(\frac{1+iY_+}{\Gamma(\nu)+i(\nu-\nu_0-\Delta(\nu))} + \frac{1+iY_-}{\Gamma(\nu)+i(\nu+\nu_0+\Delta(\nu))}\right)dx\right). \quad (26)$$

Here, $\Gamma(\nu)$ and $\Delta(\nu)$ denote the speed-dependent pressure broadening and shift parameters, As discussed below Eq. (7) the positive- and negative-frequency resonances have the same width and opposite shift; intuitively their line mixing parameters are equal in magnitude but have an opposite sign. This couple of lines behaves as an object and its image in a mirror (see Ref.[74] and references therein). The later property can be demonstrated for any couple of pure rotational lines starting from Eq. (20) using the symmetry of the cross section (Eq. (7)) and the reduced dipole moments (Eq. (19)). At a more detailed level, one can show, using the notations introduced in Section 3.5, that $Y_{++} = -Y_{--}$ and $Y_{+-} = -Y_{-+}$, thus $Y_+ = -Y_-$.

The integral is performed over the Maxwell-Boltzmann speed distribution; $x = \frac{\nu}{\nu_m}$, where ν and ν_m are the active molecule speed and its most probable speed. To model the speed dependence of the pressure broadening and shift parameters, we used the quadratic approximation defined as [42]

$$\Gamma(\nu) = \Gamma_0 + \Gamma_2\left(x^2 - \frac{3}{2}\right), \quad (27a)$$

$$\Delta(\nu) = \Delta_0 + \Delta_2\left(x^2 - \frac{3}{2}\right), \quad (27b)$$

The two bottom panels Fig. 3 present the fully *ab initio* speed dependent pressure broadening and shift (continuous black lines) and their quadratic approximations (continuous red lines) for the CO-Ar system. Thin blue lines denote the Maxwell-Boltzmann distribution of the active molecule velocity. γ_0^{Ar} and δ_0^{Ar}, marked with dashed horizontal lines, are the speed-averaged pressure-independent spectral line-shape parameters, obtained from averaging the collisional cross sections [6]. γ_2^{Ar} and δ_2^{Ar}, which quantify the speed dependence, are calculated using the condition that the quadratic function has the same slope as the *ab initio* speed dependence at the most probable speed of the active molecule [42]. These four line-shape coefficients are reported in Table II. The line-shape parameters are the sums of the fully *ab initio* CO – Ar collisional coefficients and of the CO – CO coefficients weighed by partial pressures (see the convention defined in Eqs. (21) and (22)). The speed dependent CO – CO coefficients for the line broadening and shifting were taken from the previous experiments [23]. The line mixing effect was never studied in the pure rotational band of CO, so we utilized the same value of Y for modeling both CO – Ar and CO – CO collisions. This can be justified by the following reasoning. The value is in a reasonable agreement with data from Ref. [75] (which is for the 2-0 band). The divergence between Y parameters for the 2-0 and 0-0 bands should not be large because of the weak dependence of the collisional cross-section within small vibrational excitations. Potential impact of inaccuracy of the used value is expected to be negligible because of (i) weakness of the effect at present experimental conditions, (ii) relatively small amount of CO in the sample and (iii) insignificant difference in y coefficients for pure- and foreign-pressure broadening lines [75]. To verify this statement we doubled the related value of y in the model. The modification led to an increase of the observed minus calculated spectrum rRMSE by 0.03%.

The same approach was used for the spectra modeling at intermediate and low pressures discussed below.

3.6.2. Intermediate- and low-pressure collisional regime

This section describes the spectral line-shape model that we used to validate our *ab initio* theoretical calculations on the data from radioacoustic detection and video spectrometers. Since their principle of operation relied on the frequency modulation technique, with precisely known deviation, the experimental profiles have a dispersive shape,

$$I(\nu) = I_{VP}(\nu + \delta\nu) - I_{VP}(\nu - \delta\nu), \quad (28)$$

where $\delta\nu$ is the frequency deviation value. As the pressure gets lower, the line is significantly narrower and the factor $\left(\frac{\nu}{\nu_0}\right)^2 \approx 1$. Similarly, the influence of the negative peak present in the VVW model can be neglected. In the intermediate- and low- pressure regimes the collisional broadening no longer dominates over the Doppler broadening and both effects are taken into account within the framework of the speed-dependent Voigt profile (with inclusion of the line mixing) [10,76],

$$I_{VP}(\nu) = \frac{2}{\nu_D}\pi^{-\frac{3}{2}} Re\left(\int_0^\infty e^{x^2}\frac{x}{i} \ln\left(\frac{\Gamma_{\Omega_R}(\nu) - i(\nu-\nu_0-\Delta(\nu)) + i\nu_D x}{\Gamma_{\Omega_R}(\nu) - i(\nu-\nu_0-\Delta(\nu)) - i\nu_D x}\right)dx\right). \quad (29)$$

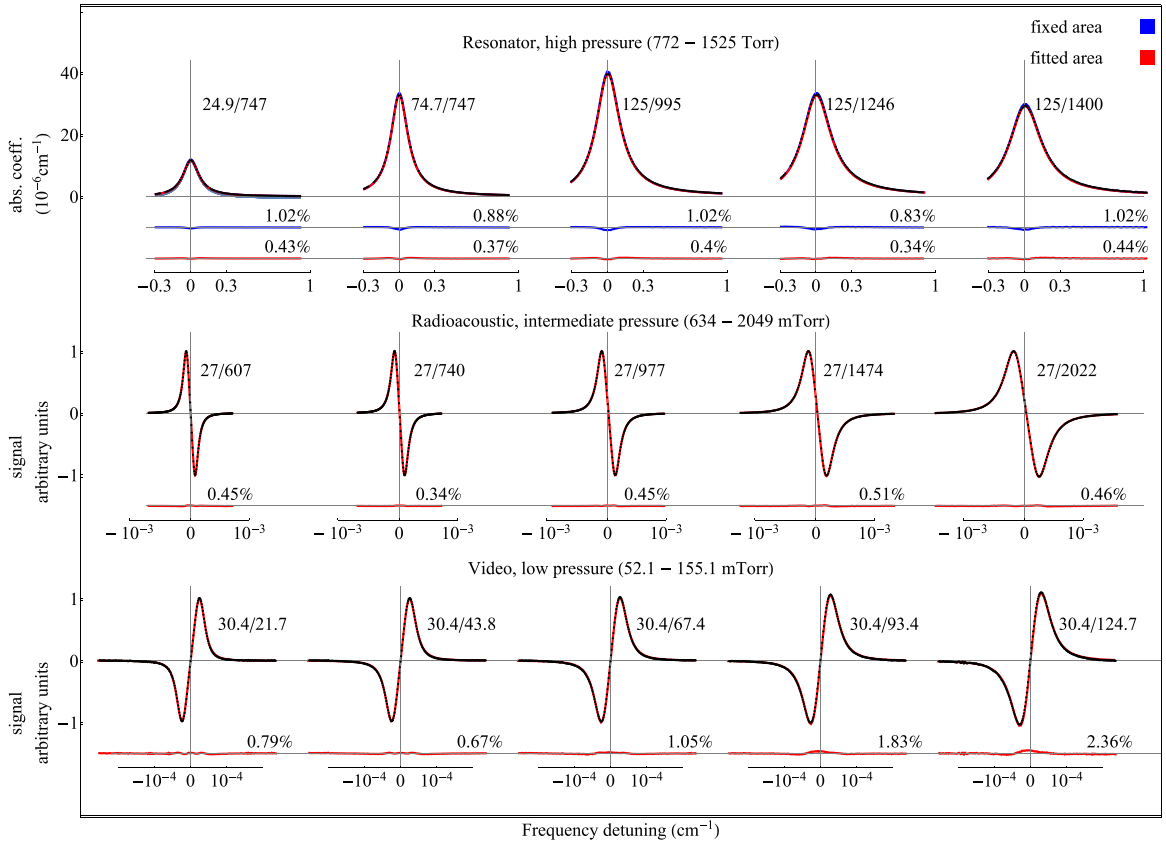

Fig. 5. Direct validation of the *ab initio* quantum-scattering calculations (performed on the PES of Cybulski [16]) on accurate experimental spectra of the R(0) line in CO perturbed by collisions with Ar atoms. The three panels from the bottom to the top show the results obtained with the three spectrometers in a very wide range of pressures from 52 mTorr to 1525 Torr (exact values of the CO and Ar pressures are given above each profile; the first/second value corresponds to the CO/Ar pressure). All the three spectrometers measure the absorption coefficient $\alpha(\upsilon)$, which is directly seen in the case of a resonator spectrometer (top panel). In the cases of radioacoustic and video detection spectrometers (middle and bottom panels), the line profiles have dispersive shapes due to the frequency demodulation techniques relevant for these spectrometers, see Section 2. The black dots are the experimental spectra and the red lines are the *ab initio* profiles. In the case of a resonator spectrometer (the top panel), the absolute vertical scale is accessible and the synthetic *ab initio* profiles can be generated based on the line intensity taken from the best literature value [78,79], see the blue lines (for the red lines, the line intensity was fitted). The differences between the experimental and *ab initio* profiles are shown below each graph with respective color notation. To quantify how well the theory agrees with experiments, we report for each profile the relative (with respect to the profile peak value) root mean square errors (rRMSE) of the experiment-theory differences calculated within the ±FWHM range around the line center, see the numbers (in percent) above the residuals. The spectra were acquired at $T \approx 297$ K (resonator spectrometer), $T \approx 299.35$ K (radioacoustic detection spectrometer), and $T \approx 298.15$ K (video spectrometer). (For interpretation of the references to colour in this figure legend, the reader is referred to the web version of this article.)

The effective broadening parameter

$$\Gamma_{\Omega_R}(\upsilon) = \sqrt{(\Gamma(\upsilon))^2 + \Omega_R^2} \tag{30}$$

includes the Rabi frequency Ω_R characterizing transition saturation by a radiation power. It can be determined as a product of the amplitude of the electric field of the radiation and matrix element of the transition dipole moment [77]. Under conditions of our study with radioacoustic spectrometer, Ω_R was estimated for the R(0) line as 0.11–0.13 MHz, which is comparable to the Doppler half-width. For video spectrometer recordings, the Rabi frequency was about an order of magnitude lower. While the role of the Doppler effect is pronounced only in the lowest pressure range, one could expect the Dicke narrowing effect to play a role. To estimate its influence, we compared the simplest Dicke-narrowed speed-dependent Hard Collision profile [1] with the speed-dependent Voigt profile. In the considered pressure regime, the two models differ on the level of 0.05% (the relative root-mean-square error calculated within ± FWHM of the line profile, rRMSE=0.05%), which is much smaller than the systematic uncertainty related to the choice of PES, and hence we neglect the Dicke narrowing.

4. Direct comparison of the *ab initio* synthetic profiles with the measured spectra

Having performed both the *ab initio* calculations and accurate line-shape measurements, we compare our synthetic line-shape profiles with the experimental results in Fig. 5. In each of the 15 spectra presented in Fig. 5 the line-shape parameters are fixed to our *ab initio* values (obtained from Cybulski's PES [16]). The top panel presents five absorption profiles measured with the resonator spectrometer in our highest pressure range (772–1525 Torr). We compared the experimental data with the *ab initio* calculations by adjusting only the baseline and slope (*i.e.*, constant and linear with the frequency terms added to the line shape model) to compensate for the possible effect of unaccounted far line wings together with an absorption by molecular pairs (bimolecular absorption) and fixing the intensity parameter to the best literature value [78,79], see the blue curves in Fig. 5. We also performed an alternative analysis, adjusting the intensity parameter individually for each line to focus only on the collisional line-shape effects and exclude intensity uncertainty, see the red residuals on the top panel of Fig. 5.

Similarly, to compare the *ab initio* data with experimental results collected with the radioacoustic detection and video spectrometers, we performed a multi-spectrum fitting procedure, ad-

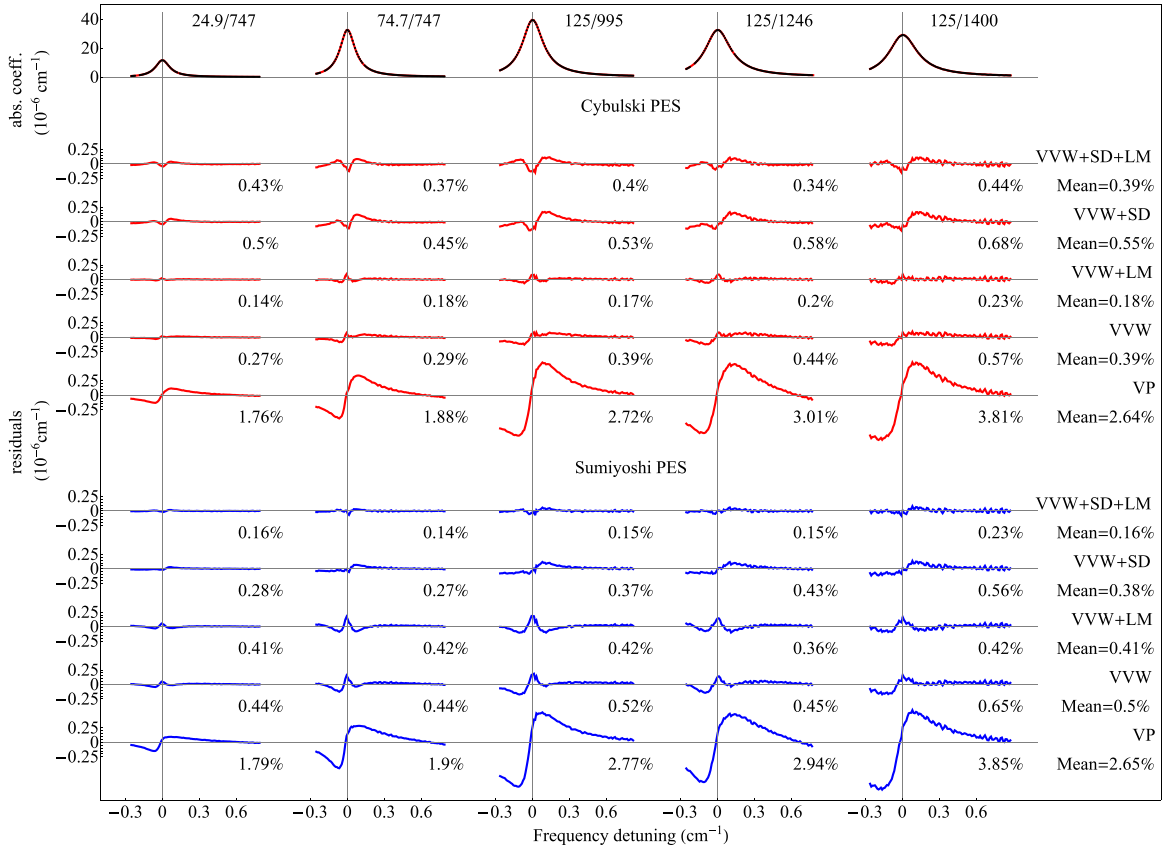

Fig. 6. Comparison of the absolute differences between theoretical and experimental spectra (red lines and black dots on the top panel) collected with a resonator spectrometer for different line-shape models and PESs. The ten lower panels present how taking into account different collisional effects influences the agreement with experimental data. The results displayed with red lines are the absolute residuals calculated using the Cybulski's PES [16], while the blue lines correspond to the results obtained with the Sumiyoshi's PES [41]. The absolute differences between the *ab initio* synthetic data and the experimental spectra are accompanied by relative root mean square errors (rRMSE) of the experiment-theory differences calculated within the ±FWHM range around the line center, see the numbers (in percent) above the residuals. In the right part of the figure we list the abbreviations we used for the profiles (VP=Voigt Profile, VVW=van Vleck-Weisskopf Profile, LM=line mixing, and SD=speed dependence of the collisional broadening and shift), as well as the mean rRMSE resulting from the use of the given model. Since we did not calculate the Y parameter for Sumiyoshi's PES, the contribution of LM in each case is based on Cybulski's PES. (For interpretation of the references to colour in this figure legend, the reader is referred to the web version of this article.)

justing Ω_R (which depends on apparatus settings). These techniques do not give direct access to the absolute line intensities; therefore we adjusted the intensity of each line separately. To account for the apparatus effect relevant for the radioacoustic and video spectrometers, we fitted a frequency-proportional scaling factor, as well as the baseline and slope. Five lines measured with a radioacoustic spectrometer in the intermediate-pressure range (634-2049 mTorr) are displayed on the middle panel of Fig. 5 together with the corresponding theoretical data. Similarly, five spectra collected with a video spectrometer in the low-pressure regime (52.1–155.1 mTorr), accompanied by their theoretical counterparts are located on the bottom panel of Fig. 5.

The absorption corresponding to other lines of CO spectrum is small, but not negligible in the frequency range under study. This additional absorption was modeled as follows and subtracted from experimental spectra before their comparison with *ab initio* profiles. The van Vleck-Wesskopf line shape function was used with an additional term taking into account the line mixing effect in the first order of pressure (so-called Rosenkranz profile [67]). The far wings of the profile were truncated at 25 cm^{-1} detuning from its maximum as suggested in [80]. The line-by-line sum of such profiles was calculated for all (excluding the studied one) rotational lines of CO isotopologues in the ground and vibrational states with integrated intensities larger than 10^{-28} cm/molec following the HITRAN2016 line list and using line intensities and self-broadening coefficients from this database [81]. Ar-broadening coefficients were adopted from [47], assuming the same rotational dependence and independence on vibrational state. The rotational dependence of the line mixing parameters was evaluated on the basis of our ECSA off-diagonal relaxation elements. Then the line mixing coefficients for all rotational lines (excluding the R(0) line) were calculated by scaling this dependence using the R(0) line coefficient value calculated in this work and reported in Table 2.

Below each of the 15 spectra displayed in Fig. 5, we present absolute residuals, *i.e.*, differences between theoretical and experimental data. As was mentioned in the previous paragraph, two sets of residuals are displayed on the top panel, corresponding to the analysis with fitted (red curves) and fixed (blue curves) line intensity. Each residual is accompanied by the value of the relative root mean square error (rRMSE, expressed in %) to quantify the agreement between theoretical and experimental data.

In the case of the resonator spectrometer data, we obtained percent-level rRMSE when the area was fixed to the database value, while adjusting it brought residuals below 0.5 % for each of the five lines. In the case of the radioacoustic spectrometer data, the agreement between theoretical and experimental lines expressed in terms of rRMSE was at a level of 0.5 %. The situation was much different in the case of the video spectrometer data. Indeed, the studied pressure range included a region where the effect of baseline fluctuations is not negligible. Among 106 scans, we

selected a series of five, sharing the same Rabi frequency, whose baseline fluctuations were the smallest. The remaining baseline deformation, due to the apparatus, was reduced by subtracting a third-order polynomial from the raw data. Ultimately, we achieved a rRMSE within 0.7- 2.3 %, which was dominated by the apparatus effect, and not by the *ab initio* calculations.

In the next step of our analysis, we examined how neglecting different line-shape effects can affect the agreement between theoretical and experimental data for the case of a resonator spectrometer. Fig. 6 presents a direct comparison of ten different approaches to model the line shape profile. In this case, the line intensity was a fitting parameter. Similarly to the convention applied in Fig. 5, each residual curve is followed by the numerical value of rRMSE. Additionally, the performance of each model is summarized in the right part of the picture by the mean rRMSE. The figure shows two sets of data, either obtained by using Cybulski's PES [16] (red residuals), or by using Sumiyoshi's PES [41] (blue residuals). For comparison, we begin with the simple Voigt profile (VP), which is conventional for the IR and visible spectral ranges, where the condition $\nu_0 \gg$ HWHM is strictly fulfilled. A significant improvement is observed after employing the van Vleck-Weisskopf profile (VVW) confirming its superiority for broad lines in the microwave range [82]. A 1.7 % difference between two PESs in Γ_0 (see Table II) becomes notable at this step. Taking into account the line mixing (LM) effect leads to an even better agreement between theory and experiment for both PESs (recall that the LM parameter is determined from scattering calculations performed on Cybulskis PES.) At this step we see that something is still missing. W-shape residuals that are characteristic for the SD effect manifestation are seen for both PESs. Now, if we disregard the LM, but just take into account the SD effect, the residuals show the asymmetric skew typical for the LM effect, which is more prominent for Sumiyoshi's PES. This step improves the agreement as compared to a simple VVW analysis in the case of Sumiyoshi's PES, but worsens the agreement for Cybulski's PES. Note that the theoretical SD of the width and shift (the latter plays an insignificant role in our case) are very similar for both PESs and the 1.7 % difference in widths become crucial. Clearly, the role of the LM is preponderate over the SD broadening at the highest pressures. The final SDVVWLM profile accounting for both effects shows the best agreement with the experimental data for Sumiyoshi's PES, while this is not the case for Cybulski's PES. On the one hand, this result seemingly demonstrates the advantage of the Sumiyoshi PES and could be tentatively explained as a slight underestimation of the line width using Cybulski's PES, thus compensating the line narrowing due to the SD effect. On the other hand, we should admit that there are other influencing issues leading either to the theoretical underestimation of the width or to the additional line broadening due to some experimental artifact, which may compensate for the inaccuracy of Sumiyoshis PES and thus hide the advantage of the Cybulskis PES. Therefore, we avoid any judgment on which of the two PESs is more accurate and conclude that the influence of SD effect is of the same order as influence of PESs (around 0.2 %), which is similar to overall accuracy we reach in our ultimate comparison.

5. Discussion and conclusions

The results gathered in Figs. 5 and 6 show that our theoretical *ab initio* calculations predict the collision-perturbed shapes of the spectral lines to the sub-percent level. The most broadband spectra were collected with a resonator spectrometer. These spectra are the most advantageous for our goal because of (i) the absolute vertical scale in units of absorption coefficient, which allows to fix the line intensity, (ii) the clear manifestation of the line mixing effect, and (iii) the smallest impact from the apparatus contributions. These spectra are in 0.15-0.38% agreement with the *ab initio* calculations, depending on the chosen PES. We also achieved a 0.4% level of accuracy for spectra recorded with radioacoustic spectrometer in the intermediate-pressure range. The residuals in the low-pressure regime are dominated by the apparatus effect and do not allow us to state the agreement at the same level of accuracy. However, the experimental data still reveal good agreement with theoretical profiles, implying that our *ab initio* calculations are valid in a wide pressure range, spanning 50 mTorr to 1500 Torr.

The very good agreement between theoretical and experimental data obtained at room temperature allows us to assert that the same level of accuracy of our *ab initio* calculations can be expected within a quite broad range of temperatures. This follows from the fact that the calculations are performed on a grid of kinetic energies covering a range between 0.1 and 2000 cm^{-1}, corresponding to about 1.5 - 2800 K in terms of thermal energy k_BT. To demonstrate such a capability we provide in Appendix B the results of calculation of line shape parameters calculation for a number of temperatures within this range. This additional data may be helpful for future experimental or theoretical works, as well as for population of spectroscopic databases.

Thus, using the example of the R(0) line of the ground vibrational state of CO molecules colliding with Ar, we have demonstrated that the state-of-the-art *ab initio* calculations are able to reproduce the observed shape of atmospherically relevant molecules at a sub percent level of uncertainty, which is quite sufficient for most present day applications.

Declaration of Competing Interest

The authors declare that they have no known competing financial interests or personal relationships that could have appeared to influence the work reported in this paper.

CRediT authorship contribution statement

E.A. Serov: Investigation, Formal analysis. **N. Stolarczyk:** Formal analysis, Writing - review & editing. **D.S. Makarov:** Formal analysis, Data curation. **I.N. Vilkov:** Investigation. **G. Yu. Golubiatnikov:** Investigation, Methodology. **A.A. Balashov:** Investigation. **M.A. Koshelev:** Investigation, Methodology. **P. Wcisło:** Methodology, Writing - original draft. **F. Thibault:** Investigation, Writing - original draft. **M. Yu. Tretyakov:** Conceptualization, Supervision.

Acknowledgments

Experiment was supported in parts by the Russian State project (0030-2021-0016) and Russian Science Foundation (17-19-01602). Financial support from RFBR project No. 18-55-16006 is acknowledged. P.W. was supported by National Science Centre, Poland, Project No. 2018/31/B/ST2/00720. N.S. was supported by National Science Centre, Poland, Project No. 2019/35/B/ST2/01118. The project was co-financed by the Polish National Agency for Academic Exchange under the PHC Polonium program (dec. PPN/X/PS/318/2018).

Appendix A. The complex Dicke parameter

Other effects due to collisions affect the line shape. Hess [3], a long time ago, approximated the collision operator by two relaxation frequencies, $\tilde{\omega}_A$ and $\tilde{\omega}_R$ (the generalized Hess parameters). By doing so, he solved a semi-classical kinetic equation which takes into account the internal motion and the drift term due to the translational motion leading to the Dicke narrowing. This theory was later on completed [53,54] essentially by making a link with the formalism in Liouville space and the scattering matrix leading to a close coupling expression of the generalized Hess spectroscopic cross sections (Eq. (6)). Following the generalized Hess

notations, the complex pressure broadening and shift coefficient is denoted as

$$\tilde{\omega}_A = \Gamma - i\Delta = n_b\ \tilde{\omega}_0^{00}(q). \tag{A.1}$$

The quantity $\tilde{\omega}_R$ takes into account the correlation between the translational and internal motions and is expressed in terms of two, mass weighted collision integrals,

$$\tilde{\omega}_R = n_b \frac{m_a}{m_a + m_b} \tilde{\omega}_0^{00}(q) \ + \ \frac{2}{3} n_b \frac{m_b}{m_a + m_b} \tilde{\omega}_1^{11}(q). \tag{A.2}$$

These collision integrals are in turn derived from the GHM cross sections,

$$\tilde{\omega}_\lambda^{s,s'}(q) = \bar{\nu}_r \int dx x^{(s+s'+2)/2} e^{-x} \sigma_\lambda^q(E_{kin} = x k_B T). \tag{A.3}$$

Making the link between Hess profile [3] and various profiles that take into account the Dicke narrowing [1,2], some of us recognized [6] that the frequency of the velocity changing collisions is indeed

$$\tilde{\nu}_{opt} \equiv \tilde{\omega}_R - \tilde{\omega}_A. \tag{A.4}$$

In the following, we call $\tilde{\nu}_{opt}$ the complex Dicke parameter [14,15]. Note that this parameter contributes both to the broadening and shift of a line because it is complex valued.

Appendix B. Temperature dependence of the line shape parameters

This Appendix describes the temperature dependence of the spectral line-shape parameters of the R(0) line of CO in Ar. For simplicity, we omit the Ar superscript within this section, as the CO-CO parameters are excluded from this discussion. We performed fully *ab initio* line-shape calculations to obtain the set of spectroscopic coefficients γ_0, δ_0, γ_2, δ_2, $\tilde{\nu}^{\rm r}_{\rm opt}$, $\tilde{\nu}^{\rm i}_{\rm opt}$, and $y^{\rm r}$ at temperatures between 100 and 700 K. Table B.4 provides the pressure broadening and shift coefficients, as well as the complex Dicke parameter and the real part of the line mixing coefficient for selected temperatures between 10 and 700 K. Between 77 and 300 K we estimate an error of the order of 0.5% for these data. Below 25 K the error maybe of the order of a few percents due to the resonances that may appear in the kinetic energy dependent cross sections. At 700 K we may have an error of this order, too, due to the methods of quadrature used and extrapolation above $E_{kin} = 2000$ cm^{-1} (see Eq. (A.3)).

Table B.4
Line shape parameters for the pure rotational R(0) line of CO in argon and for selected temperatures: pressure broadening coefficients (γ_0), pressure shift coefficients (δ_0), real and imaginary parts of the complex Dicke parameter ($\tilde{\nu}_{opt}$), and the real part of the line mixing coefficient (y). The units are 10^{-3} cm^{-1} atm^{-1} (except y, which is in 10^{-3} atm^{-1}). The first entries are obtained with Cybulski's PES [16] and the second ones with Sumiyoshi's PES [41].

T(K)	γ_0	δ_0	$\tilde{\nu}^{\rm r}_{\rm opt}$	$\tilde{\nu}^{\rm i}_{\rm opt}$	$y^{\rm r}$
10	975.25	0.08	123.58	14.73	-1.32
	1016.00	2.58	121.22	-2.62	
25	467.45	4.92	58.93	4.38	1.73
	476.48	3.90	57.90	1.12	
50	274.20	2.98	34.05	0.68	4.66
	276.75	2.10	35.16	-0.05	
77	197.60	1.54	24.20	-0.14	5.83
	199.37	1.13	25.21	-0.35	
100	162.00	0.88	19.58	-0.26	6.18
	163.67	0.65	20.40	-0.35	
150	118.80	0.23	13.90	-0.21	6.11
	120.40	0.14	14.45	-0.23	
195	96.98	0.01	11.05	-0.14	5.72
	98.50	-0.04	11.45	-0.15	
240	82.50	-0.08	9.20	-0.09	5.26
	83.93	-0.11	9.52	-0.09	
273	74.60	-0.11	8.22	-0.06	4.94
	75.94	-0.14	8.50	-0.07	
297	69.80	-0.12	7.63	-0.05	4.71
	71.10	-0.14	7.88	-0.05	
400	55.21	-0.13	5.92	-0.01	3.90
	56.35	-0.14	6.05	-0.01	
500	46.30	-0.11	4.87	0.00	3.30
	47.25	-0.12	4.90	0.00	
600	40.05	-0.09	4.05	0.00	2.85
	40.85	-0.10	3.98	0.00	
700	35.35	-0.07	3.27	0.00	2.49
	36.00	-0.08	3.15	0.00	

The double-power-law (DPL) temperature dependence of the spectral line-shape parameters adopted in the HITRAN database [13,42] is defined by the following equation:

$$X(T) = \sum_{i=1}^{2} \mathrm{Coeff}_i \left(\frac{T_{ref}}{T} \right)^{\mathrm{Exp}_i}, \tag{B.1}$$

where X stands for any particular line-shape parameter, $T_{\rm ref}$ is 296 K, and Coeff_i and Exp_i are the numerical coefficients. The DPL representation of the temperature dependence of the real part

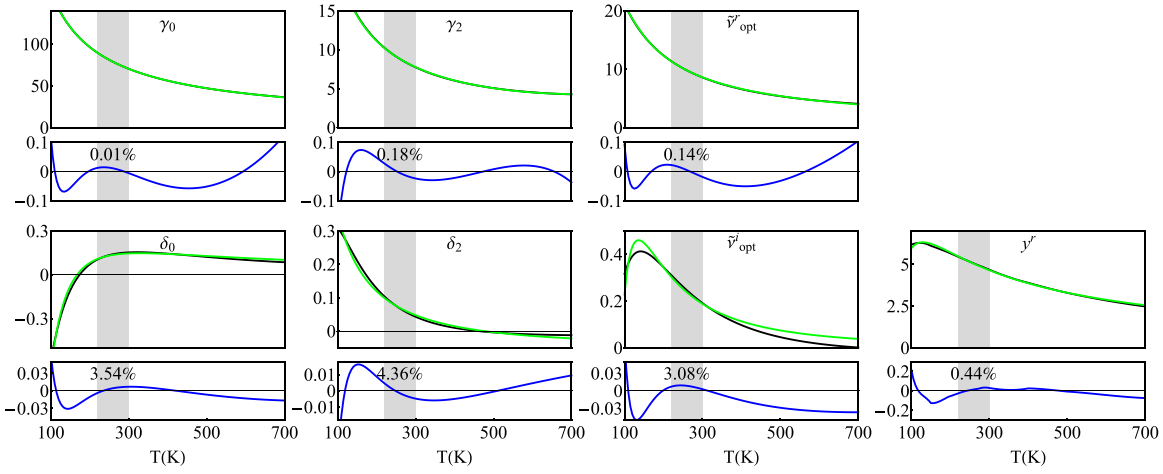

Fig. B.7. Temperature dependences of the spectral line-shape parameters of the R(0) line of CO in Ar. For simplicity, we omit the Ar superscripts in this figure. Each of the seven main plots presents the *ab initio* (black curves) and their double-power-law (DPL) representations [42] (green curves). The units of the vertical axes of the plots are 10^{-3}cm^{-1}atm^{-1}, except for the y^r coefficient having the unit of 10^{-3}atm^{-1}. Below each graph we show residuals, as well as the relative root-mean-square value of the residuals in the prioritized temperature range (the area between 220 and 300K marked with gray background), normalized by the mean value of the corresponding line-shape coefficient in this range. (For interpretation of the references to colour in this figure legend, the reader is referred to the web version of this article.)

Table B.5
The parameters of the DPL representation of the CO-Ar R(0) line-shape parameters. The units of coefficients 1 and 2 are 10^{-3}cm^{-1}atm^{-1} (except for $\bar{y}$ and $\bar{y}'$ in units of 10^{-3}atm^{-1}) and exponents 1 and 2 are dimensionless. All the DPL coefficients are defined by Eq. (B.1), following the original formulation from Ref. [42].

parameter	Coeff$_1$	Coeff$_2$	Exp$_1$	Exp$_2$
γ_0(T)	-1.0319	72.2319	1.8536	0.7946
δ_0(T)	100.34175	-100.48787	1.47913	1.47659
γ_2(T)	0.0147	7.8418	-4.4324	0.8909'
δ_2(T)	-4.048	4.098	0.696	0.721
$\tilde{\nu}^r_{opt}$(T)	-0.1	8.816	3.13	0.926
$\tilde{\nu}^i_{opt}$(T)	-19.892	20.085	2.5151	2.5069
y^r(T)	-651.20	655.89	1.1897	1.1854

of the line-mixing parameter, Y^r has not yet been considered in the HITRAN database. Nonetheless, we applied the DPL function Eq. (B.1) to the Y parameter similarly to the other line-shape parameters.

Fig. B.7 presents a comparison of our *ab initio* data with their DPL representations. While adjusting the DPL function to the *ab initio* data, we performed a weighted fitting procedure, prioritizing the temperature range corresponding to the terrestrial atmosphere (between 220 and 300 K, marked with gray areas in Fig. B.7; we used $\times$10 weights in this range). Below each of the seven graphs, we plot absolute residuals and give the relative root mean square error (rRMSE) in the prioritized temperature range, normalized by the mean value of the considered line-shape parameter in the prioritized range. While the accuracy achieved for the γ_0, γ_2 and $\tilde{\nu}^r_{\rm opt}$ is on the per mile level or better (0.01% for γ_0), the values of rRMSE values for δ_0, δ_2, and $\tilde{\nu}^i_{\rm opt}$ are relatively high due to the low value of the normalization factor in the denominator. Table B.5 contains the set of coefficients required to reconstruct the DPL parameterization of our R(0) line defined by Eq. (B.1).

References

[1] Hartmann J-M, Boulet C, Robert D. Collisional effects on molecular spectra. Amsterdam: Elsevier; 2008.
[2] Hartmann J-M, Tran H, Armante R, Boulet C, Campargue A, Forget F, Gianfrani L, Gordon I, Guerlet S, Gustafsson M, Hodges JT, Kassi S, Lisak D, Thibault F, Toon GC. Recent advances in collisional effects on spectra of molecular gases and their practical consequences. J Quant Spectrosc Radiat Transfer 2018;213:178–227.
[3] Hess S. Kinetic theory of spectral line shapes. the transition between Doppler broadening and collisional broadening. Physica 1972;61:80–94.
[4] Schaefer J, Köhler W. Quantum calculations of rotational and NMR relaxation, depolarized Rayleigh and rotational Raman line shapes for H2(HD)–He mixtures. Physica A 1985;129:469.
[5] Demeio L, Green S, Monchick L. Effects of velocity changing collisions on line shapes of HF in Ar. J Chem Phys 1995;102:9160–6. doi:10.1063/1.468864.
[6] Thibault F, Patkowski K, Żuchowski PS, Jóźwiak H, Ciuryło R, Wcisło P. Rovibrational line-shape parameters for H2 in He and new H2-He potential energy surface. J Quant Spectrosc Radiat Transfer 2017;202:308.
[7] Blackmore R. A modified Boltzmann kinetic equation for line shape functions. J Chem Phys 1987;87:791.
[8] Ciuryło R, Shapiro DA, Drummond JR, May A. Solving the line-shape problem with speed-dependent broadening and shifting and with Dicke narrowing. II. application. Phys Rev A 2002;65:012502.
[9] May A, Liu W-K, McCourt F, Ciuryło R, Stoker JS-F, Shapiro D, Wehr R. The impact theory of spectral line shapes: a paradigm shift. Can J Phys 2013;91:879.
[10] Wcisło P, Thibault F, Zaborowski M, Wójtewicz S, Cygan A, Kowzan G, Masłowski P, Komasa J, Puchalski M, Pachucki K, Ciuryło R, Lisak D. Accurate deuterium spectroscopy for fundamental studies. J Quant Spectrosc Radiat Transfer 2018;213:41.
[11] Jóźwiak H, Thibault F, Stolarczyk N, Wcisło P. Ab initio line-shape calculations for the S and O branches of H_2 perturbed by He. J Quant Spectrosc Radiat Transfer 2018;219:313–22. doi:10.1016/j.jqsrt.2018.08.023.
[12] Słowiski M, Thibault F, Tan Y, Wang J, Liu A-W, Hu S-M, Kassi S, Campargue A, Konefał M, Jówiak H, Patkowski K, Żuchowski P, Ciuryło R, Lisak D, Wcisło P. H_2–He collisions: *Ab initio* theory meets cavity-enhanced spectra. Phys Rev A 2020;101:052705.
[13] Wcisło P, Thibault F, Stolarczyk N, Jóźwiak H, Słowinski M, Gancewski M, Stankiewicz K, Konefał M, Kassi S, Campargue A, Tan Y, Wang J, Patkowski K, Ciuryło R, Lisak D, Kochanov R, Rothman LS, Gordon IE. The first comprehensive dataset of beyond-Voigt line-shape parameters from *ab initio* quantum scattering calculations for the HITRAN database: He-perturbed H_2 case study. J Quant Spectrosc Radiat Transfer 2021;260:107477.
[14] Thibault F, Martnez RZ, Bermejo D, Wcisło P. Line-shape parameters for the first rotational lines of HD in He. Mol Astrophys 2020;19:100063. doi:10.1016/j.molap.2020.100063.
[15] Kowzan G, Wcisło P, Słowiski M, Masłowski P, Viel A, Thibault F. Fully quantum calculations of the line-shape parameters for the Hartmann-Tran profile: A CO-Ar case study. J Quant Spectrosc Radiat Transfer 2020;243:106803. doi:10.1016/j.jqsrt.2019.106803.
[16] Kowzan G, Cybulski H, Wcisło P, Słowiński M, Viel A, Masłowski P, Thibault F. Subpercent agreement between ab initio and experimental collision-induced line shapes of carbon monoxide perturbed by argon. Phys Rev A 2020;102:012821. doi:10.1103/PhysRevA.102.012821.
[17] Winnewisser G, Belov SP, Klaus T, Schieder R. Sub-Doppler measurements on the rotational transitions of carbon monoxide. J Mol Spectrosc 1997;184:468–72.
[18] Read WG, K W Hillig I, Cohen EA, Pickett HM. The measurement of absolute absorption of millimeter radiation in gases: the absorption of CO and O2. IEEE Trans Antennas Propag 1988;36:1136–43.
[19] Mader H, Guarnieri A, Doose J, Nissen N, Markov VN, Shtanyuk AM, Andrianov AF, Shanin VN, Krupnov AF. Comparative studies of $J-J=1-0$ CO line parameters in frequency and time domains. J Mol Spectrosc 1996;180:183–7.
[20] Markov VN, Mader H. Pressure self-shift of the $J=1-0$ line of carbon monoxide. J Mol Spectrosc 2001;205:350–2. doi:10.1006/jmsp.2000.8277.
[21] Yamada K, Abe H. The line broadening and shift effects on the CO $J=5-4$ transition at 576 GHz induced by collisions with rare gases. J Mol Spectrosc 2003;217:87–92.
[22] Colmont J-M, Nguyen L, Rohart F, Wlodarczak G. Lineshape analysis of the $J=3-2$ and $J=5-4$ rotational transitions of room temperature CO broadened by N_2, O_2, CO_2 and noble gases. J Mol Spectrosc 2007;246:86–97.
[23] Seleznev AF, Fedoseev GV, Koshelev MA, Tretyakov MY. Shape of collision-broadened lines of carbon monoxide. J Quant Spectrosc Radiat Transfer 2015;161:171–9.
[24] Thibault F, Boissoles J, Le Doucen R, Farrenq R, MorillonChapey M, Boulet C. Line-by-line measurements of interference parameters for the 0-1 and 0-2 bands of CO in He, and comparison with coupledstates calculations. J Chem Phys 1992;97(7):4623–32. doi:10.1063/1.463865.
[25] Boissoles J, Thibault F, Domenech JL, Bermejo D, Boulet C, Hartmann JM. Temperature dependence of line mixing effects in the stimulated Raman Q-branch of CO in He: a further test of close coupling calculations. J Chem Phys 2001;115(16):7420–8. doi:10.1063/1.1394752.
[26] Martínez RZ, Domenech JL, Bermejo D, Thibault F, Bouanich J-P, Boulet C. Close coupling calculations for rotational relaxation of CO in argon: Accuracy of energy corrected sudden scaling procedures and comparison with experimental data. J Chem Phys 2003;119(20):10563–74. doi:10.1063/1.1620506.
[27] Predoi-Cross A, Esteki K, Rozario H, Naseri H, Latif S, Thibault F, Malathy Devi V, Smith M, Mantz A. Theoretical and revisited experimentally retrieved He-broadened line parameters of carbon monoxide in the fundamental band. J Quant Spectrosc Radiat Transfer 2016;184:322–40. doi:10.1016/j.jqsrt.2016.08.007.
[28] Predoi-Cross A, Bouanich JP, Benner DC, May AD, Drummond JR. Broadening, shifting, and line asymmetries in the 2←0 band of CO and CO–N_2 : Experimental results and theoretical calculations. J Chem Phys 2000;113(1):158–68. doi:10.1063/1.481783.
[29] Bendana FA, Lee DD, Wei C, Pineda DI, Spearrin RM. Line mixing and broadening in the $\nu(1-3)$ first overtone bandhead of carbon monoxide at high temperatures and high pressures. J Quant Spectrosc Radiat Transfer 2019;239:106636. doi:10.1016/j.jqsrt.2019.106636.
[30] Krupnov AF, Tretyakov MY, Belov SP, Golubiatnikov GY, Parshin VV, Koshelev MA, Makarov DS, Serov EA. Accurate broadband rotational BWO-based spectroscopy. J Mol Spectrosc 2012;280:110–18. doi:10.1016/j.jms.2012.06.010.
[31] Golubiatnikov GY, Belov SP, Leonov II, Andriyanov AF, Zinchenko II, Lapinov AV, Markov VN, Shkaev AP, Guarnieri A. Precision sub-Doppler millimeter and submillimeter Lamb-dip spectrometer. Radiophys Quantum El 2014;56:599–609.
[32] Golubiatnikov GY, Belov SP, Lapinov AV. The features of the frequency-modulation method when studying the shapes of the spectral lines of nonlinear absorption. Radiophys Quantum El 2017;59:715–26. doi:10.1007/s11141-017-9740-z.
[33] Krupnov AF. Academic Press, L; 1979. p. 217–56.
[34] Tretyakov MY, Koshelev MA, Makarov DS, Tonkov MV. Precise measurements of collision parameters of spectral lines with a spectrometer with radioacoustic detection of absorption in the millimeter and submillimeter ranges. Instrum Exp Tech 2008;51(1):78–88.
[35] Koshelev MA, Tsvetkov AI, Morozkin MV, Glyavin MY, Tretyakov MY. Molecular gas spectroscopy using radioacoustic detection and high-power coherent subterahertz radiation sources. J Mol Spectrosc 2017;331:9–16. doi:10.1016/j.jms.2016.10.014.
[36] Golubiatnikov GY, Koshelev MA, Tsvetkov AI, Fokin AP, Glyavin MY, Tretyakov MY. Sub-terahertz high-sensitivity high-resolution molecular spectroscopy with a gyrotron. IEEE Trans Terahertz Sci Technol 2020;10(5):502–12. doi:10.1109/TTHZ.2020.2984459.
[37] Koshelev MA, Leonov II, Serov EA, Chernova AI, Balashov AA, Bubnov GM, et al. New frontiers in modern resonator spectroscopy. IEEE Trans Terahertz Sci Technol 2018;8:773–83.

[38] Vlasov SN, Koposova EV, Kornishin SY, Parshin VV, Perminov DA, Serov EA. Wideband windows for vacuum devices of millimeter and submillimeter wavelength ranges. Radiophys Quantum El 2020;63:106–13.

[39] Dymond JH, Marsh KN, Wilhoit RC, Wong KC. Virial coefficients of pure gases and mixtures subvolume A: virial coefficients of pure gases. Berlin, Heidelberg, New York: Springer-Verlag; 2002.

[40] Dymond JH, Marsh KN, Wilhoit RC. Virial coefficients of pure gases and mixtures subvolume B: virial coefficients of mixtures. Berlin, Heidelberg, New York: Springer-Verlag; 2003.

[41] Sumiyoshi Y, Endo Y. Three-dimensional potential energy surface of Ar — CO. J Chem Phys 2015;142:024314. doi:10.1063/1.4905268.

[42] Stolarczyk N, Thibault F, Cybulski H, Jóźwiak H, Kowzan G, Vispoel B, et al. Evaluation of different parameterizations of temperature dependences of the line-shape parameters based on ab initio calculations: case study for the HITRAN database. J Quant Spectrosc Radiat Transfer 2020;240:106676. doi:10.1016/j.jqsrt.2019.106676.

[43] Murrell JN, Sorbie KS. New analytic form for the potential energy curves of stable diatomic states. J Chem Soc, Faraday Trans 2 1974;70:1552–6. doi:10.1039/F29747001552.

[44] Huxley P, Murrell JN. Ground-state diatomic potentials. J Chem Soc, Faraday Trans 2 1983;79:323–8. doi:10.1039/F29837900323.

[45] Hutson J.M., Green S.. MOLSCAT version14, Collaborative Computational Project 6 of the UK Science and Engineering Research Council, Daresbury Laboratory, UK1995;.

[46] McBane G.C.. PMP Molscat, a parallel version of Molscat version 14, available at Grand Valley State University2005;http://faculty.gvsu.edu/mcbaneg/pmpmolscat.

[47] Luo C, Wehr R, Drummond JR, May AD, Thibault F, Boissoles J, Launay JM, Boulet C, Bouanich J-P, Hartmann J-M. Shifting and broadening in the fundamental band of CO highly diluted in He and Ar: A comparison with theory. J Chem Phys 2001;115(5):2198–206. doi:10.1063/1.1383049.

[48] Thibault F, Martínez RZ, Domenech JL, Bermejo D, Bouanich J-P. Raman and infrared linewidths of CO in Ar. J Chem Phys 2002;117(6):2523–31. doi:10.1063/1.1494975.

[49] Wehr R, Vitcu A, Ciuryło R, Thibault F, Drummond JR, May AD. Spectral line shape of the $P(2)$ transition in CO-Ar: uncorrelated ab initio calculation. Phys Rev A 2002;66:062502. doi:10.1103/PhysRevA.66.062502.

[50] Mantz AW, Thibault F, Cacheiro JL, Fernandez B, Pedersen TB, Koch H, Valentin A, Claveau C, Henry A, Hurtmans D. Argon broadening of the ^{13}CO R(0) and R(7) transitions in the fundamental band at temperatures between 80 and 297 K: comparison between experiment and theory. J Mol Spectrosc 2003;222(2):131–41. doi:10.1016/S0022-2852(03)00200-5.

[51] Wehr R, Ciuryło R, Vitcu A, Thibault F, Drummond JR, May AD. Dicke-narrowed spectral line shapes of CO in Ar: Experimental results and a revised interpretation. J Mol Spectrosc 2006;235(1):54–68. doi:10.1016/j.jms.2005.10.009.

[52] Wehr R, Vitcu A, Thibault F, Drummond JR, May AD. Collisional line shifting and broadening in the fundamental P-branch of CO in Ar between 214 and 324 K. J Mol Spectrosc 2006;235(1):69–76. doi:10.1016/j.jms.2005.10.004.

[53] Corey GC, McCourt FR. Dicke narrowing and collisional broadening of spectral lines in dilute molecular gases. J Chem Phys 1984;81:2318–29. doi:10.1063/1.447930.

[54] Monchick L, Hunter LW. Diatomic-diatomic molecular collision integrals for pressure broadening and Dicke narrowing: a generalization of Hess's theory. J Chem Phys 1986;85:713–18. doi:10.1063/1.451277.

[55] Yutsis AP, Levinson I, Vanagas VV. Mathematical apparatus of the theory of angular momentum. Jerusalem: Israel Program for Scientific Translations; 1962. doi:101007/978-3-662-10403-3.

[56] Schaefer J, Monchick L. Line shape cross sections of HD immersed in He and H_2 gas. I. Pressure broadening cross sections. J Chem Phys 1987;87:171–81. doi:10.1063/1.453612.

[57] Schaefer J, Monchick L. Line broadening of HD immersed in He and H_2 gas. A&A 1992;265:859–68.

[58] Ben-Reuven A. Impact broadening of microwave spectra. Phys Rev 1966;145:7–22. doi:10.1103/PhysRev.145.7.

[59] Shafer R, Gordon RG. Quantum scattering theory of rotational relaxation and spectral line shapes in H_2 - He gas mixtures. J Chem Phys 1973;58:5422–43. doi:10.1063/1.1679162.

[60] Fano U. Pressure broadening as a prototype of relaxation. Phys Rev 1963;131:259–68. doi:10.1103/PhysRev.131.259.

[61] Martínez RZ, Bermejo D, Thibault F, Wcisło P. Testing the ab initio quantum-scattering calculations for the D_2-He benchmark system with stimulated Raman spectroscopy. J Raman Spectrosc 2018;49(8):1339–49. doi:10.1002/jrs.5391.

[62] Lévy A, Lacome N, Chackerian C. Collisional line mixing. In: Rao KN, Weber A, editors. Spectroscopy of the Earth's Atmosphere and Interstellar Medium. Academic Press; 1992. p. 261–337. ISBN 978-0-12-580645-9. doi:10.1016/B978-0-12-580645-9.50008-3.

[63] DePristo AE, Augustin SD, Ramaswamy R, Rabitz H. Quantum number and energy scaling for nonreactive collisions. J Chem Phys 1979;71(2):850–65. doi:10.1063/1.438376.

[64] Thibault F, Boissoles J, Boulet C, Ozanne L, Bouanich JP, Roche CF, Hutson JM. Energy corrected sudden calculations of linewidths and line shapes based on coupled states cross sections: the test case of CO_2-argon. J Chem Phys 1998;109(15):6338–45. doi:10.1063/1.477187.

[65] Bonamy L, Thuet JM, Bonamy J, Robert D. Local scaling analysis of state-to-state rotational energy-transfer rates in N_2 from direct measurements. J Chem Phys 1991;95(5):3361–70. doi:10.1063/1.460841.

[66] Millot G. Rotationally inelastic rates over a wide temperature range based on an energy corrected sudden exponential power theoretical analysis of Raman line broadening coefficients and Q branch collapse. J Chem Phys 1990;93(11):8001–10. doi:10.1063/1.459329.

[67] Rosenkranz PW. Shape of the 5 mm oxygen band in the atmosphere. IEEE Trans Antennas Propag 1975;23(4):498–506. doi:10.1109/TAP.1975.1141119.

[68] Smith EW. Absorption and dispersion in the O_2 microwave spectrum at atmospheric pressures. J Chem Phys 1981;74(12):6658–73. doi:10.1063/1.441112.

[69] Boulet C, Hartmann J-M. Toward measurements of the speed-dependence of line-mixing. J Quant Spectrosc Radiat Transfer 2021;262:107510. doi:10.1016/j.jqsrt.2021.107510.

[70] Esteki K, Predoi-Cross A, Povey C, Ivanov S, Ghoufi A, Thibault F, Smith MAH. Room temperature self- and H_2-broadened line parameters of carbon monoxide in the first overtone band: theoretical and revised experimental results. J Quant Spectrosc Radiat Transfer 2017;203:309–24. doi:10.1016/j.jqsrt.2017.04.008.

[71] Ciuryło R. Shapes of pressure- and Doppler-broadened spectral lines in the core and near wings. Phys Rev A 1998;58:1029–39. doi:10.1103/PhysRevA.58.1029.

[72] Vleck JHV, Weisskopf VF. On the shape of collision-broadened lines. Rev Mod Phys 1945;17:227–36. doi:10.1103/RevModPhys.17.227.

[73] Makarov DS, Vilkov IN, Koshelev MA, Aderkina AA, Tretyakov MY. Collisional coupling of the molecular oxygen $^{16}O_2$ fine-structure lines under low pressures. Radiophys Quantum El 2018;60(10):808–23. doi:10.1007/s11141-018-9849-8.

[74] Rosenkranz P. Interference coefficients for overlapping oxygen lines in air. J Quant Spectrosc Radiat Transfer 1988;39(4):287–97. doi:10.1016/0022-4073(88)90004-0.

[75] Malathy DV, Benner DC, Smith MH, Mantz AW, Sung K, Brown LR. Spectral line parameters including temperature dependences of self- and air-broadening in the 2←0 band of CO at 2.3 μm. J Quant Spectrosc Radiat Transfer 2012;113:1013–33.

[76] Voigt W. Aber das Gesetz der Intensittsverteilurg innerhalb der Linien eines Gasspektrnms. Sitzber KB Akad Wiss Mnchen, Math-Phys Klasse 1912:603–20.

[77] Demtröder W. Laser spectroscopy: basic concepts and instrumentation. 35th. New York, NY, USA: Springer; 2008.

[78] Coxon JA, Hajigeorgiou PG. Direct potential fit analysis of the $X^1\Sigma^+$ ground state of CO. J Chem Phys 2004;121(7):2992–3008. doi:10.1063/1.1768167.

[79] Li G, Gordon IE, Rothman LS, Tan Y, Hu S-M, Kassi S, Campargue A, Medvedev ES. Rovibrational line lists for nine isotopologues of the CO molecule in the $X^1\Sigma^+$ ground electronic state. ApJS 2015;216(1):15. doi:10.1088/0067-0049/216/1/15.

[80] Clough SA, Kneizys FX, Davies RW. Line shape and the water vapor continuum. Atmos Res 1989;23:229–41.

[81] Gordon IE, Rothman LS, Hill C, Kochanov RV, Tan Y, Bernath PF, Birk M, Boudon V, Campargue A, Chance KV, Drouin BJ, Flaud J-M, Gamache RR, Hodges JT, Jacquemart D, Perevalov VI, Perrin A, Shine KP, Smith M-AH, Tennyson J, Toon GC, Tran H, Tyuterev VG, Barbe A, Csszr AG, Devi VM, Furtenbacher T, Harrison JJ, Hartmann J-M, Jolly A, Johnson TJ, Karman T, Kleiner I, Kyuberis AA, Loos J, Lyulin OM, Massie ST, Mikhailenko SN, Moazzen-Ahmadi N, Mller HSP, Naumenko OV, Nikitin AV, Polyansky OL, Rey M, Rotger M, Sharpe SW, Sung K, Starikova E, Tashkun SA, Auwera JV, Wagner G, Wilzewski J, Wcisło P, Yu S, Zak EJ. The HITRAN2016 molecular spectroscopic database. J Quant Spectrosc Radiat Transfer 2017;203:3–69. doi:10.1016/j.jqsrt.2017.06.038.

[82] Hill RJ. Water vapor-absorption line shape comparison using the 22-GHz line: the Van Vleck–Weisskopf shape affirmed. Radio Sci 1986;21/3:447–51.